Cell Reports

Resource

Interactome Mapping Provides a Network of Neurodegenerative Disease Proteins and Uncovers Widespread Protein Aggregation in Affected Brains

Graphical Abstract

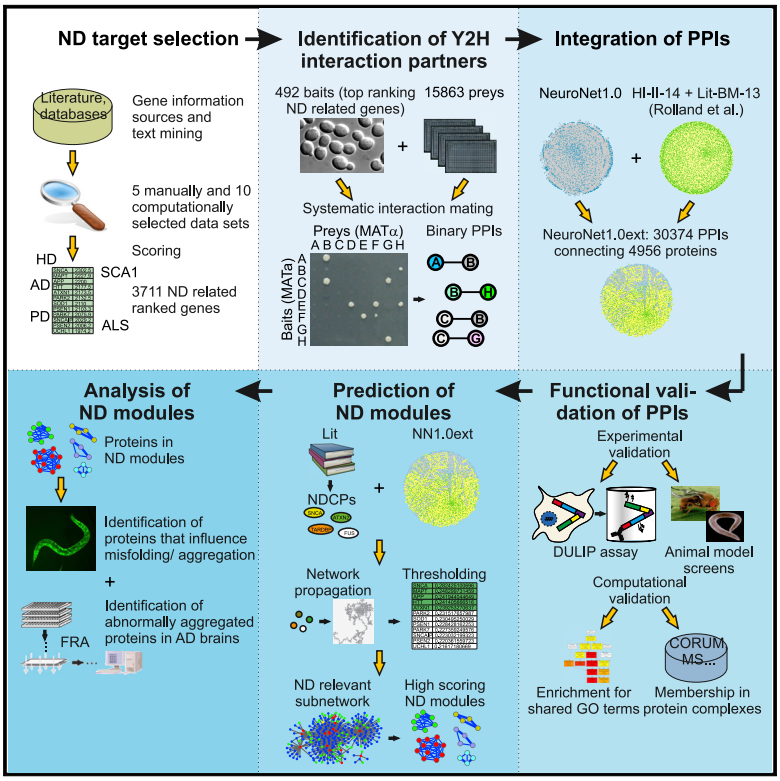

Authors

Christian Haenig, Nir Atias, Alexander K. Taylor, ..., Miguel A. Andrade-Navarro, Roded Sharan, Erich E. Wanker

Correspondence

roded@tauex.tau.ac.il (R.S.), erich.w@mdc-berlin.de (E.E.W.)

In Brief

Haenig et al. present an interactome network of ~30,000 connections among ~5,000 proteins involved in neurodegenerative diseases. The network highlights proteins that influence aggregation and toxicity of known disease-causing proteins and predicts disease-specific subnetworks and new proteins found to be abnormally aggregated in AD patient brains.

Highlights

- A map of ~30,000 connections of ~5,000 human proteins relevant to neurodegeneration
- Network approach identifies modifiers of mutant TDP-43 and HTT toxicity in flies
- ARF-GEP$_{100}$ controls misfolding and aggregation of disease-causing proteins
- MKL1 and ataxin-1 abnormally aggregate in AD patient brains

Haenig et al., 2020, Cell Reports *32*, 108050
August 18, 2020
https://doi.org/10.1016/j.celrep.2020.108050

CellPress

Cell Reports

CellPress
OPEN ACCESS

Resource

Interactome Mapping Provides a Network of Neurodegenerative Disease Proteins and Uncovers Widespread Protein Aggregation in Affected Brains

Christian Haenig,[1] Nir Atias,[2] Alexander K. Taylor,[3] Arnon Mazza,[2] Martin H. Schaefer,[5,7] Jenny Russ,[1,11] Sean-Patrick Riechers,[1,11] Shushant Jain,[8] Maura Coughlin,[3] Jean-Fred Fontaine,[5,6] Brian D. Freibaum,[3] Lydia Brusendorf,[1] Martina Zenkner,[1] Pablo Porras,[1,10] Martin Stroedicke,[1] Sigrid Schnoegl,[1] Kristin Arnsburg,[9] Annett Boeddrich,[1] Lucia Pigazzini,[9] Peter Heutink,[8] J. Paul Taylor,[3,4] Janine Kirstein,[9] Miguel A. Andrade-Navarro,[5,6] Roded Sharan,[2,*] and Erich E. Wanker[1,12,*]

[1]Neuroproteomics, Max Delbrück Center for Molecular Medicine, 13125 Berlin, Germany
[2]School of Computer Science, Tel-Aviv University, Tel-Aviv 69978, Israel
[3]Department of Cell and Molecular Biology, St. Jude Children's Research Hospital, Memphis, TN 38105-3678, USA
[4]Howard Hughes Medical Institute, Chevy Chase, MD 20815-6789, USA
[5]Division of Computational Biology and Data Mining, Max Delbrück Center for Molecular Medicine, 13125 Berlin, Germany
[6]Institute of Organismic and Molecular Evolution, Johannes Gutenberg University of Mainz, 55122 Mainz, Germany
[7]Computational Cancer Biology, European Institute of Oncology, 20141 Milano, Italy
[8]DZNE Tübingen and Eberhard Karls Universität Tübingen, 72076 Tübingen, Germany
[9]Leibniz-Forschungsinstitut für Molekulare Pharmakologie (FMP) im Forschungsverbund Berlin e.V., 13125 Berlin, Germany
[10]EMBL-EBI, Wellcome Genome Campus, Hinxton, Cambridgeshire CB10 1SD, UK
[11]These authors contributed equally
[12]Lead Contact
*Correspondence: roded@tauex.tau.ac.il (R.S.), erich.w@mdc-berlin.de (E.E.W.)
https://doi.org/10.1016/j.celrep.2020.108050

SUMMARY

Interactome maps are valuable resources to elucidate protein function and disease mechanisms. Here, we report on an interactome map that focuses on neurodegenerative disease (ND), connects ~5,000 human proteins via ~30,000 candidate interactions and is generated by systematic yeast two-hybrid interaction screening of ~500 ND-related proteins and integration of literature interactions. This network reveals interconnectivity across diseases and links many known ND-causing proteins, such as α-synuclein, TDP-43, and ATXN1, to a host of proteins previously unrelated to NDs. It facilitates the identification of interacting proteins that significantly influence mutant TDP-43 and HTT toxicity in transgenic flies, as well as of ARF-GEP$_{100}$ that controls misfolding and aggregation of multiple ND-causing proteins in experimental model systems. Furthermore, it enables the prediction of ND-specific subnetworks and the identification of proteins, such as ATXN1 and MKL1, that are abnormally aggregated in postmortem brains of Alzheimer's disease patients, suggesting widespread protein aggregation in NDs.

INTRODUCTION

Neurodegenerative diseases (NDs), such as Alzheimer's disease (AD), Parkinson's disease (PD), Huntington's disease (HD), amyotrophic lateral sclerosis (ALS), and frontotemporal dementia (FTD), are seriously disabling, chronic disorders that put an enormous burden on patients, caregivers, and health systems (Goedert, 2015; Ross et al., 2014; Taylor et al., 2016). Disease-modifying treatments are urgently needed; existing therapies target symptoms in the late stages of disease, when pathology is already advanced and relief is modest (Bawa et al., 2016). To find effective treatments, it is of critical importance to understand the underlying molecular mechanisms responsible for onset and progression of NDs (Keiser et al., 2016; Khanam et al., 2016).

Decades of research have revealed commonalities between inherited and sporadic NDs (Ling et al., 2013). This includes overlapping clinical symptoms, pathway perturbations, and pathogenic molecular mechanisms, like aggregation of disease-relevant proteins (Higashi et al., 2007; Rubinsztein, 2006). Databases and network models have been created that enable the identification of relevant pathways, common genetic modifiers (Chen and Burgoyne, 2012; Khurana et al., 2017; Na et al., 2013), and proteins linked to known ND-associated proteins (Lim et al., 2006; Limviphuvadh et al., 2007).

The deposition of misfolded proteins in inclusion bodies or amyloid plaques, both inside and outside of neuronal and glial cells, is a pathological hallmark of more than 15 NDs, including AD, PD, FTD, ALS, and polyglutamine (polyQ) disorders such as HD (Chiti and Dobson, 2006; Jellinger, 2012). Although the

main protein component of pathological aggregates is specific to each disease, such as α-synuclein (SNCA) in PD, huntingtin (HTT) in HD, and β-amyloid in AD, several pathogenic proteins are known to misfold and aggregate in more than one disease. Abnormal aggregation of the RNA binding protein TDP-43 is observed in FTD, ALS, and several further conditions (Chen-Plotkin et al., 2010; Toyoshima and Takahashi, 2014). Similarly, the anomalous aggregation and deposition of SNCA and tau is a pathological phenomenon detectable in brains of patients with AD, PD, HD, and dementia with Lewy bodies (Gratuze et al., 2016; Jellinger, 2012). This overlap in protein pathology supports the hypothesis that neuronal dysfunction and degeneration in various NDs are caused by shared pathomechanisms (Ling et al., 2013). This view is substantiated by more recent discoveries indicating that amyloid aggregates from β-amyloid, tau, HTT, SNCA, and TDP-43 polypeptides are biologically active structures that can self-replicate and spread from cell to cell by a prion-like mechanism (Brettschneider et al., 2015; Soto, 2012). Such corruptive aggregation templates, often termed seeds, might function as drivers of pathogenesis in various NDs.

Studies of protein-protein interactions (PPIs) have demonstrated that size, shape, and physicochemical complementarities are critical determinants of protein complex formation (Pechmann et al., 2009). Hydrophobic and electrostatic interactions are further driving forces of aberrant protein aggregation (Tartaglia et al., 2008). Identifying and characterizing PPIs can therefore provide valuable knowledge on the formation of aberrant protein aggregates and the cellular processes that control them. The aggregation propensity of ND-associated proteins such as HTT is influenced dramatically by interactions with other proteins (Stroedicke et al., 2015). PPIs either accelerate or slow aggregation kinetics, thereby influencing toxicity of disease-causing proteins in model systems (Mogk and Bukau, 2017; Morley et al., 2002).

To identify connections between proteins, quantitative affinity purification/mass spectrometry (MS)-based methods (Hosp et al., 2015) or yeast-two-hybrid (Y2H) assays (Arumughan et al., 2016; Goehler et al., 2004) are of high utility. They can detect not only high-affinity PPIs but also weak, transient interactions (Hein et al., 2015). These may have particular relevance when aggregation-prone proteins are studied, because these are often intrinsically disordered (Uversky et al., 2008) and bind only weakly to partner proteins (Shimizu and Toh, 2009). Disordered proteins, widespread in the human proteome (Pentony and Jones, 2010; Uversky et al., 2008), are enriched among known ND-associated proteins (Raychaudhuri et al., 2009), suggesting that as a group they may play crucial roles in ND processes.

Recent theoretical investigations indicate that a large fraction of the proteins in the human proteome are vulnerable to misfolding and aggregation because their cellular concentrations relative to their solubilities are high (Ciryam et al., 2013, 2015). These supersaturated or metastable proteins are overrepresented in pathways perturbed in NDs (Ciryam et al., 2013). Many proteins besides the known ones (HTT, SNCA, tau, TDP-43, etc.) may therefore be aberrantly aggregated in disease brains. They need to be identified to assess their relevance for pathogenesis.

In this study, we performed a systematic Y2H interaction screen and integrated publicly available interaction data to generate a high-confidence interactome map (~5,000 proteins connected via ~30,000 candidate interactions) for ND-associated human proteins. Our network uncovers interconnectivity across NDs and links known ND-causing proteins (NDCPs), such as SNCA, TDP-43, and ataxin-1 (ATXN1), to proteins previously believed to be unrelated to NDs. It facilitated the identification of interacting proteins that significantly influence mutant TDP-43 and HTT toxicity in transgenic fly models. Furthermore, it enabled the detection of the protein ARF-GEP$_{100}$ that controls misfolding and aggregation of multiple disease proteins in experimental models. Finally, disease-specific subnetworks of AD, PD, and ALS (AD$_{SN}$, PD$_{SN}$, and ALS$_{SN}$) were predicted and proteins such as MKL1 and ATXN1 were found to be aggregated in AD postmortem brain tissue. Our focused interactome map provides a powerful framework for elucidating the underlying mechanisms of multiple NDs.

RESULTS

Selection of Bait Proteins and Automated Interaction Screening

We used manually and computationally generated gene lists to prioritize human protein-encoding genes for their association with NDs such as AD, PD, ALS, HD, and SCA1 (Figure 1A; Table S1). By systematically extracting and combining information on diseases from available public databases and PubMed abstracts (Fontaine et al., 2009, 2011), a ranked list of 3,711 genes with a potential role in NDs was generated (Table S1). The 100 top-ranking genes include many well-known ND genes, such as *SNCA*, *MAPT*, *APP*, *HTT*, and *ATXN1*. These genes, when mutated, cause early-onset, inherited NDs with severe symptoms (Gatchel and Zoghbi, 2005; Taylor et al., 2016). Importantly, a fraction of the top 100 genes have not been studied extensively in the context of NDs so far (Figure S1; Table S1).

To identify interaction partners for proteins involved in multiple NDs, an automated Y2H system was applied, which allows the detection of binary PPIs through systematic interaction mating (Stelzl et al., 2005; Vinayagam et al., 2011). We focused on the first 524 open reading frames (ORFs) from the ranked list. They were subcloned as full-length cDNAs or fragments thereof into bait expression plasmids using the Gateway technology. We generated 596 MATa yeast strains that produce DNA binding domain fusion proteins (baits), of which 492 (82.6%) (Table S1) produced non-autoactivating bait proteins and were suitable for interaction mating. Subsequently, all MATa strains were screened as pools against an array of ~16,000 MATα yeast strains expressing prey proteins. Positive clones, which activate the reporters *HIS3*, *URA3*, and *lacZ*, were identified by growth selection on selective plates and β-galactosidase assays (Figure 1B). To increase our sampling, the entire search space was independently screened four times. Putative interactions identified in the pooled mating experiments were subsequently retested in multiple pairwise experiments. The steps of the automated interaction mating procedure are summarized in Figure S2A.

CellPress
OPEN ACCESS

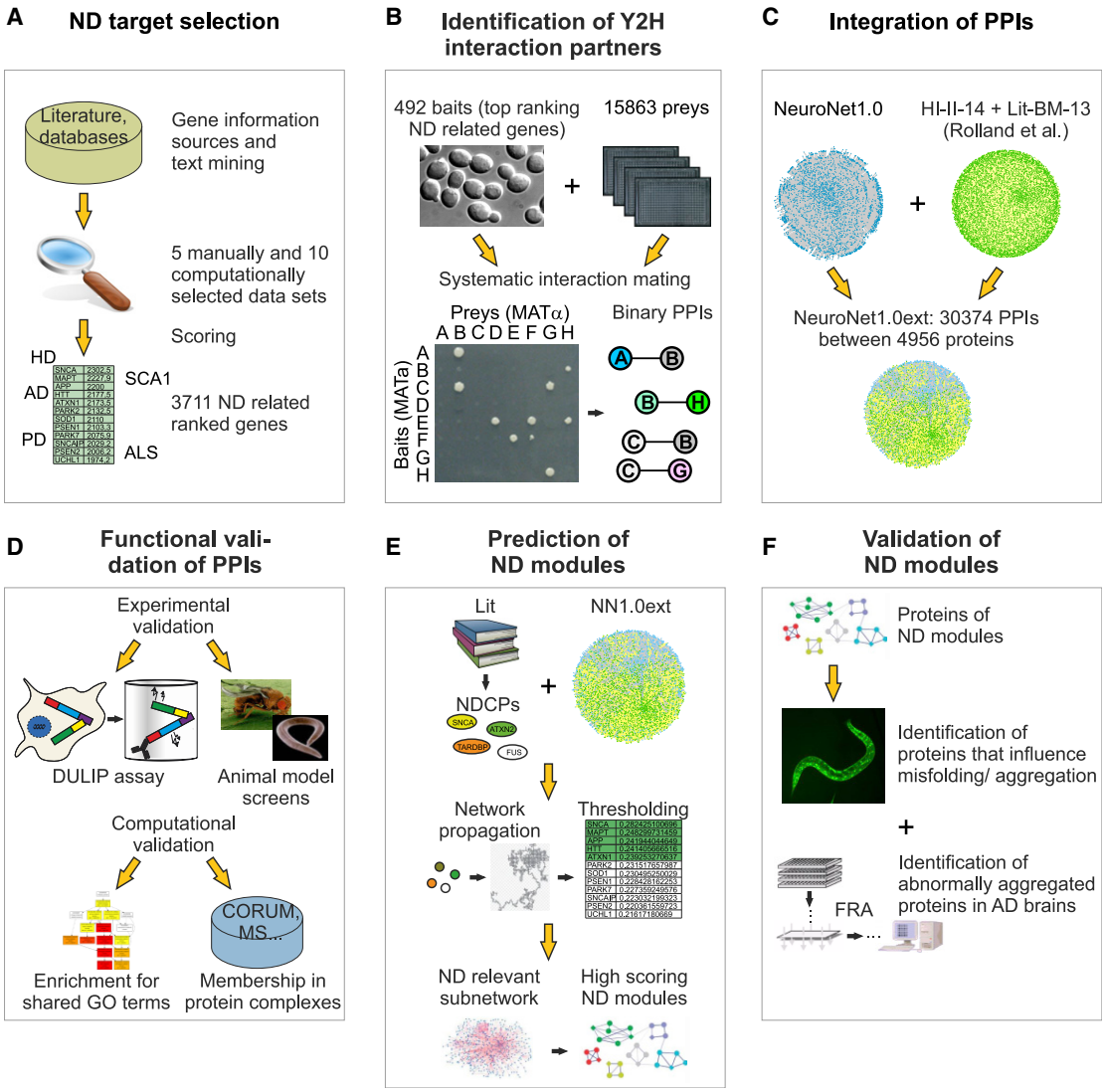

Figure 1. Research Approach and Workflow of the Interactome Mapping Study

(A) Selection of ND-associated target proteins for interaction mapping studies using available literature information.

(B) Identification of interaction partners for selected target proteins by automated Y2H interaction screening.

(C) Integration of identified Y2H interactions with published binary PPIs to create an extended interactome network for proteins involved in NDs.

(D) Validation of selected binary PPIs with computational and experimental methods.

(E) Computational prediction of subnetworks and protein modules for AD, PD, and ALS starting from NN1.0ext and known NDCPs.

(F) Analysis of the potential disease relevance of selected proteins from computationally predicted ND modules using experimental model systems and patient brain samples.

See also Tables S1, S2, S3, S4, S5, and S6 and Figures S2 and S4–S6.

Using this experimental approach, we identified 18,663 Y2H candidate interactions connecting 471 bait and 3,482 prey proteins. For further analysis of PPI data, each cDNA fragment was mapped to the Entrez GeneID and a final dataset—termed NeuroNet1.0 (NN1.0)—was created. It connects 3,135 unique human proteins via 13,736 Y2H PPIs (Table S2). A comparison of the NN1.0 data with literature interactions in the HIPPIE (Human Integrated Protein–Protein Interaction rEference) database (Alanis-Lobato et al., 2017) revealed that only 783 (~5.7%) of the identified PPIs are already known.

Extension of NN1.0 and Computational Validation of Y2H Interactions

Because previous investigations with positive PPI reference sets have demonstrated that the sensitivity of Y2H assays is ~25% (Venkatesan et al., 2009), it is advisable to combine high-confidence binary interaction datasets to augment the scope and density of interactome network maps. To expand NN1.0 (Figure 1C), we added high-quality binary interactions from the Lit-BM-13 and HI-II-14 datasets (Rolland et al., 2014). Using this strategy, we created NeuroNet1.0extended (NN1.0ext) that

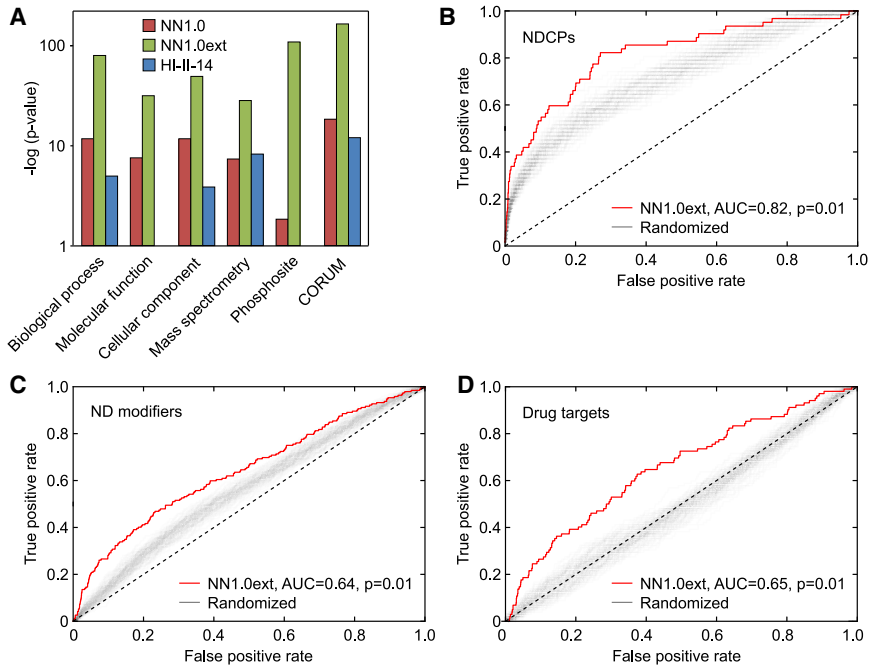

Figure 2. Functional and Disease Relevance of Binary Interactions in NN1.0 and NN1.0ext

(A) Enrichment of binary interactome maps (NN1.0, NN1.0ext, and HI-II-14) for functional relationships and cocomplex memberships. Literature interactions were obtained from previous publications and databases: HI-II-14, binary interactome dataset; MS, MS-based map; Phosphosite, kinase-substrate interactions; CORUM, protein complex dataset.

(B–D) Prediction of known NDCPs, ND modifiers, and drug targets in NN1.0ext using network propagation. Prediction performance is measured using a ROC curve (red); predictions were compared with those of 100 randomized networks that preserve node degrees (gray) and the random expectation (dashed black).

See also Table S3.

either directly connects NN1.0 proteins or links Lit-BM-13 and HI-II-14 proteins to NN1.0 proteins (Figure S2B) via at least two interactions. NN1.0ext links 4,956 human proteins via 30,374 candidate interactions (Table S2).

Next, we performed a computational assessment of the quality of the interactions in NN1.0 and NN1.0ext. The high-quality PPI dataset HI-II-14 (Rolland et al., 2014) was analyzed as a control. We first measured enrichment for shared Gene Ontology (GO) terms for biological process (BP), molecular function (MF), and cellular component (CC). We observed significant enrichment for BP and CC terms in all three datasets (Figure 2A). For MF, significant enrichment was observed for NN1.0 and NN1.0ext, but not for HI-II-14. Then, we determined how many binary interactions are part of larger protein complexes as annotated in CORUM (protein complex data set) (Ruepp et al., 2010) and MS (Woodsmith and Stelzl, 2014), a MS-based interaction dataset. We observed similar performance of the PPIs from all three datasets (Figure 2A). Finally, we investigated the overlap of the interactions in the three datasets with kinase-substrate interactions cataloged in Phosphosite (Hornbeck et al., 2015). We found that interactions from both NN1.0 and NN1.0ext, but not from HI-II-14, were enriched, indicating that the ND-focused datasets contain known kinase-substrate interactions. Overall, these results support the assumption that NN1.0 and NN1.0ext contain biologically meaningful interactions.

Finally, we assessed the network's relevance for known NDCPs, such as SNCA, HTT, and TDP-43. In NN1.0ext, 2,173 proteins are linked to 94 known NDCPs (Tables S2 and S3). 62 NDCPs are connected via 85 direct interactions (Figure S2C), suggesting that NDs are linked at the molecular level. Using a cross-validation setting, we assessed the ability of NN1.0ext to predict novel proteins relevant for ND. Starting from curated sets of (1) NDCPs, (2) known ND modifiers, and (3) drug targets (Table S3), we used a network propagation algorithm (Vanunu et al., 2010) to predict ND-related proteins. For comparison, the same procedure was applied to 100 randomized networks with the same node degree distribution. Receiver operating characteristic (ROC) curve analysis revealed that NN1.0ext is suited to predict NDCPs, ND modifiers, and drug targets (Figures 2B–2D; empirical $p < 0.01$).

Experimental Validation of Interactions

For experimental validation (Figure 1D), Y2H interactions were retested in a dual luminescence-based coimmunoprecipitation (DULIP) assay in mammalian cells (Trepte et al., 2015). We first assessed the performance of the method with two reference sets, one with known low-affinity PPIs (dissociation constant Kd > 10^{-7} M; L-Aff reference set), another with known high-affinity PPIs (Kd < 10^{-7} M; H-Aff reference set). In addition, the reference sets hsPRS-v1 and hsRRS-v1 (Braun et al., 2009) were investigated. We detected PPIs in the reference sets L-Aff and H-Aff with success rates of 26.5% and 39.1%, respectively (Figure 3A; Table S4), substantiating previous observations that coimmunoprecipitation methods have a preference for high-affinity interactions (Elion, 2006). In comparison, PPIs in the reference sets hsPRS-v1 and hsRRS-v1 were identified with success rates of 30.5% and 3.8%, respectively (Figure 3A; Table S4), confirming that the method is suited to distinguishing between positive and negative interactions (Trepte et al., 2015). Next, we applied the DULIP method to independently validate 231 randomly selected PPIs from the NN1.0ext dataset, of which 169 (73.2%) were NN1.0 PPIs. We confirmed the NN1.0 interactions with a success rate of 23.1% (39 PPIs), whereas the interactions from the HI-II-14 dataset (62 PPIs) were detected with a success rate of 25.8% (16 PPIs). Altogether, we confirmed Y2H interactions in NN1.0ext with a success rate of 23.8% (55 PPIs) (Figure 3A; Table S4), indicating that the data can be verified with DULIP to a similar extent as the L-Aff interactions.

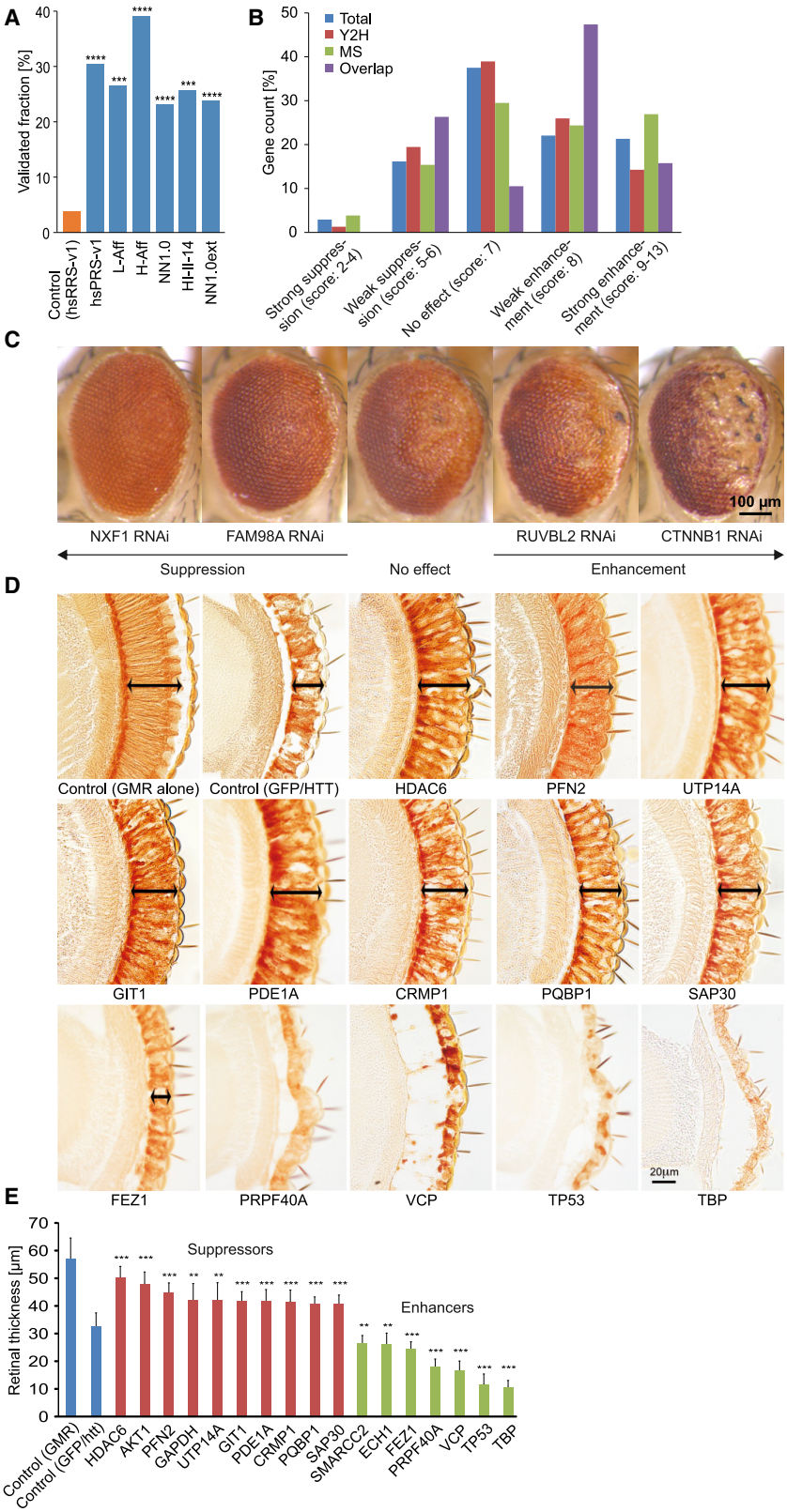

Figure 3. Experimental Validation of Interactions in DULIP Assays and Disease Model Systems

(A) Validation of binary Y2H PPIs in mammalian cells using DULIP. The recovery of binary interactions by DULIP from several PPI sets was investigated. The statistical significance was assessed using a Fisher's exact test with Holm-Bonferroni correction (***p < 0.001, ****p < 0.0001).

(B) RNAi screen as an orthologous approach to assess the functional significance of TDP-43 interactions. PPIs from the NN1.0ext dataset (Y2H) and a published affinity-purification-based MS dataset were assessed with systematic RNAi knockdown experiments in a *D. melanogaster* disease model (Ritson et al., 2010).

(C) Selected eye phenotypes resulting from RNAi knockdown experiments in transgenic flies expressing the mutant protein TDP-43-M337V in photoreceptors (Ritson et al., 2010). Both phenotype enhancing and phenotype suppressing effects can be observed.

(D) Selected eye phenotypes resulting from overexpression of human HTT partner proteins in a *D. melanogaster* HD model. Expression of the mutant protein HTT336Q128 leads to a severe eye phenotype (Stroedicke et al., 2015) that can be modified by HTT-interacting proteins.

(E) Quantification of retinal degeneration in HD transgenic flies (Stroedicke et al., 2015). n ≥ 9 flies per genotype; data are represented as mean ± SEM; ***p ≤ 0.001, two-sided t test with unequal variance. Red, suppressors; green, enhancers.

See also Table S4.

To investigate whether the Y2H interactions identified in this study are of functional relevance, we performed systematic RNA interference (RNAi) knockdown experiments in a *Drosophila melanogaster* model that expresses a TDP-43 protein with the M337V mutation (Ritson et al., 2010). In humans, this mutation causes highly penetrant familial ALS (Sreedharan et al., 2008); in transgenic flies, expression of TDP-43-M337V leads to a moderate degenerative eye phenotype (Ritson et al., 2010).

We hypothesized that decreasing the abundance of biologically relevant TDP-43 interaction partners in TDP-43-M337V-expressing transgenic flies with RNAi might reveal disease-relevant functional interactions. We obtained RNAi lines (Dietzl et al., 2007) for 77 TDP-43 interaction partners (Table S4) identified in Y2H screens and crossed these lines with transgenic TDP-43-M337V flies. Then, the impact of gene knockdowns on the rough-eye phenotype was systematically analyzed. For most genes, we investigated the effect of two independent RNAi lines (Table S4). Finally, fly strains were classified according to the impact of the short hairpin RNAs (shRNAs) (no effect, weak effect, or strong effect). Of 77 genes tested in flies, 47 (61%) influenced the phenotype (Figures 3B and 3C). Knockdown of 12 genes (15.6%) had a strong effect on the TDP-43-M337V-mediated eye phenotype. These results are in good agreement with previous studies, indicating that modifier genes are identified with a success rate of ~45% when interaction partners of a specific target protein are assessed with focused RNAi experiments in transgenic flies (Kaltenbach et al., 2007). In comparison, in a large-scale RNAi knockdown screen in *Drosophila*, genetic modifiers were detected with a hit rate of ~7.5% (Lamitina et al., 2006; Sigoillot and King, 2011). Strikingly, our studies revealed that knockdown of the nuclear RNA export protein NXF1 strongly suppresses the TDP-43-M337V-mediated eye phenotype (Figure 3C), supporting recent observations that inhibiting TDP-43 translocation from the nucleus into the cytoplasm is a protective strategy (Archbold et al., 2018).

Similar results were obtained when the knockdown of TDP-43 interaction partners previously identified by affinity purification and MS (Freibaum et al., 2010) was analyzed in transgenic flies. We selected 78 TDP-43-interacting proteins from published data for gene knockdown experiments in TDP-43-M337V flies, of which 19 (24.4%) were also identified as TDP-43 partners in this Y2H study (Figure S3A). 55 of the genes (70.5%) influenced the rough-eye phenotype (Figures 3B and 3C). In total, the impact of 136 genes (Table S4) was systematically tested in the transgenic fly model, of which 85 genes (62.5%) influenced the TDP-43-M337V-induced rough-eye phenotype (Figures 3B, 3C, and S3B; Table S4). Knockdown of 59 genes (69.4%) enhanced the phenotype; knockdown of 26 genes (30.6%) suppressed it.

Next, the effect of interaction partners on the subcellular localization of a YFP (yellow fluorescent protein)-tagged TDP-43-M337V fusion protein was assessed in a *Caenorhabditis elegans* model. We randomly selected 15 TDP-43-interacting proteins from the Y2H interaction dataset, of which 17 orthologous genes (Table S4) were ultimately assessed in RNAi experiments (Nollen et al., 2004). We defined three phenotypes to study the gene knockdown effects on TDP-43-M337V-YFP localization: (1) exclusively nuclear localization (no effect), (2) nuclear localization plus the appearance of cytoplasmic TDP-43 protein (weak effect), and (3) nuclear localization plus cytoplasmic foci and diffuse cytoplasmic staining (strong effect). We found that knockdown of 7 (41.2%) of 17 tested genes alters the localization of TDP-43-M337V-YFP in *C. elegans* (Figure S3C; Table S4).

Finally, we assessed whether coexpression of HTT-interacting proteins can modulate a severe degenerative eye phenotype in a transgenic *D. melanogaster* HD model (Kaltenbach et al., 2007; Stroedicke et al., 2015). We generated 35 fly strains that coproduce HTT-interacting proteins and an N-terminal HTT fragment with a pathogenic polyQ tract of 128 glutamines (HTT336Q128) and investigated the degeneration of photoreceptors in flies (Stroedicke et al., 2015). We found that 17 (48.6%) of 35 investigated human proteins significantly influence the HTT336Q128-induced eye phenotype (Figures 3D and 3E; Table S4), of which 10 (58.8%) suppressed and 7 (41.2%) enhanced the phenotype. Collectively, these experiments indicate that genetic modifiers are enriched in the PPI dataset.

Prediction of ND-Focused Protein Subnetworks and Cross-Validation with Reported Datasets

Previous work has shown the utility of network-based approaches in predicting potentially disease-relevant subnetworks and protein modules (Barabási et al., 2011). To define ND-specific protein subnetworks in NN1.0ext, we applied a computational method for associating protein complexes with ND phenotypes (Mazza et al., 2016). We first scored proteins in NN1.0ext based on their proximity to a set of prior proteins, which we predefined based on their causative role in inherited NDs. We focused on AD, PD, and ALS, for which many NDCPs have been reported (Lill, 2016; Rosenberg et al., 2016; Taylor et al., 2016). Through network propagation (Cowen et al., 2017; Vanunu et al., 2010), ranked lists of network proteins were created (Figure S4A; Table S5). For each disease, the resulting propagation scores were compared with scores from random controls, which were obtained with random protein sets of the same size as the set of disease-causing proteins. Proteins with significantly high scores ($p < 0.01$) were used to create the disease subnetworks AD_{SN}, PD_{SN}, and ALS_{SN}, which contain 738, 285, and 283 human proteins (Table S5), respectively. The subnetwork ALS_{SN} is exemplarily shown in Figure S4B. It contains 13 known ALS-associated NDCPs that were initially used as priors for network propagation (Figure S4C), as well as 59 further known disease-associated proteins referenced in OMIM (OMIM disease-associated proteins [ODAPs]) (Amberger et al., 2015). Similarly, the subnetworks AD_{SN} and PD_{SN} contain NDCPs (Figure S4C), along with numerous ODAPs (Figure S4D).

Next, we performed cross-validation using two datasets with reported genetic modifiers (Chen and Burgoyne, 2012; Na et al., 2013) that influence ND-associated phenotypes in model systems such as *Drosophila*, *C. elegans*, and yeast. To identify modifiers that potentially influence pathogenesis in different NDs, we compiled the predicted proteins in AD_{SN}, PD_{SN}, and ALS_{SN} and cross-compared the generated protein list with the reported datasets (Na et al., 2013; Chen and Burgoyne, 2012). We found a significant overlap between the datasets

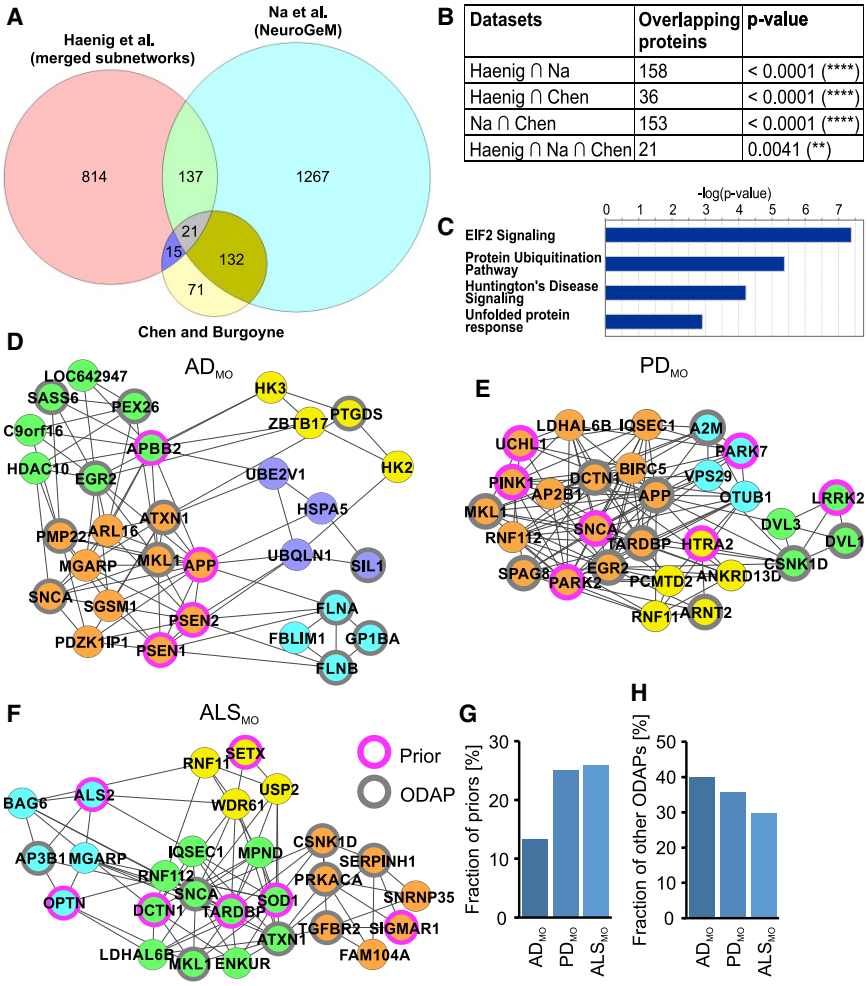

B	Datasets	Overlapping proteins	p-value
	Haenig ∩ Na	158	< 0.0001 (****)
	Haenig ∩ Chen	36	< 0.0001 (****)
	Na ∩ Chen	153	< 0.0001 (****)
	Haenig ∩ Na ∩ Chen	21	0.0041 (**)

Figure 4. Computationally Predicted ND Subnetworks and Modules

(A) Cross-comparison of computationally predicted proteins in AD_{SN}, PD_{SN}, and ALS_{SN} with datasets of potential genetic modifiers reported in Na et al. (2013) and Chen and Burgoyne (2012). The Venn diagram indicates the number of genetic modifiers recovered.

(B) Statistical analysis of data cross-comparisons. The calculated hypergeometric p values for the recovered genetic modifiers in (A) are shown.

(C) Ingenuity pathway analysis (IPA) with 21 potential genetic modifiers identified by data cross-comparison shown in (A).

(D–F) Disease protein modules containing interconnected high-scoring protein clusters for the diseases AD, PD, and ALS are shown. Known NDCPs, marked in purple, were used as a starting point (priors) for network propagation. Other known ODAPs are marked in gray. Other colors indicate highly connected protein clusters.

(G) Representation of priors (known NDCPs) in the predicted modules.

(H) Representation of other known ODAPs (based on available OMIM data) in the predicted modules. See also Table S5 and Figure S4A.

Computational Prediction of Small Experimentally Accessible Interconnected ND-Associated Protein Modules

Using an algorithm, smaller protein clusters were derived from the large subnetworks that are more easily accessible for experimental validation (Figure S4A). The generated modules AD_{MO}, PD_{MO}, and ALS_{MO} contain 30, 28, and 27 proteins, respectively (Table S5). For each disease, the 4–5 highest-scoring interconnected protein clusters are displayed (Figures 4D–4F). As expected, each module contains NDCPs that were initially used as a starting point for the module identification process (Figure 4G) as well as ODAPs (Figure 4H), which were not used as priors (Figure 4H; hypergeometric $p < 0.0001$).

Certain known NDCPs were present in multiple ND-associated protein modules. For example, ATXN1, which is mutated in SCA1 (Donato et al., 2012), was found both in AD_{MO} and ALS_{MO} (Figures 4D and 4F), supporting previous observations that *ATXN1* is also associated with these diseases (Conforti et al., 2012; Zhang et al., 2010). Similarly, we found that SNCA, which in its mutated form causes familial PD (Xu et al., 2015), is present in AD_{MO}, PD_{MO}, and ALS_{MO} (Figures 4D–4F). Proteins not previously associated with NDs, such as MKL1, a transcriptional coactivator for the serum response factor (Scharenberg et al., 2010), were linked to AD, PD, and ALS (Figures 4D–4F). Loss of this protein was previously shown to decrease neurite length in hippocampal neurons (Knöll et al., 2006). Similarly, we observed that knockdown of *Drosophila Mkl1* dramatically enhances the TDP-43-M337V-mediated rough-eye phenotype in transgenic flies (Table S4), supporting its protective role in

(Figures 4A and 4B), indicating that potential disease modifiers are present in the computationally predicted subnetworks. 21 proteins were identified in all three datasets (Figure 4A), suggesting that at least a fraction of the predicted ND-associated proteins are common disease modifiers. Many proteins initially found as genetic modifiers in HD model systems are also linked to AD pathogenesis (Table S5). For example, the ribosomal proteins L18 and L19 were found in all three predicted subnetworks (Table S5), hinting at an important role of ribosome function and/or protein translation in different NDs. In addition, Hsp40 (DNAJB4) was identified in all three subnetworks (AD_{SN}, PD_{SN}, and ALS_{SN}) (Table S5), supporting previous studies that chaperones safeguard proteostasis in different NDs (Brehme et al., 2014). A potential disease-modifying role of protein translation in NDs was confirmed by ingenuity pathway analysis (Thomas and Bonchev, 2010), indicating that proteins involved in eukaryotic Initiation Factor 2 (eIF2) signaling are enriched among the potential ND-associated genetic modifiers (Figure 4C). Strikingly, enhanced concentrations of stress kinases such as PKR (protein kinase R) that phosphorylate eIF2 and thereby slow translation have been observed in brains of ND patients (Bando et al., 2005; Hugon et al., 2017).

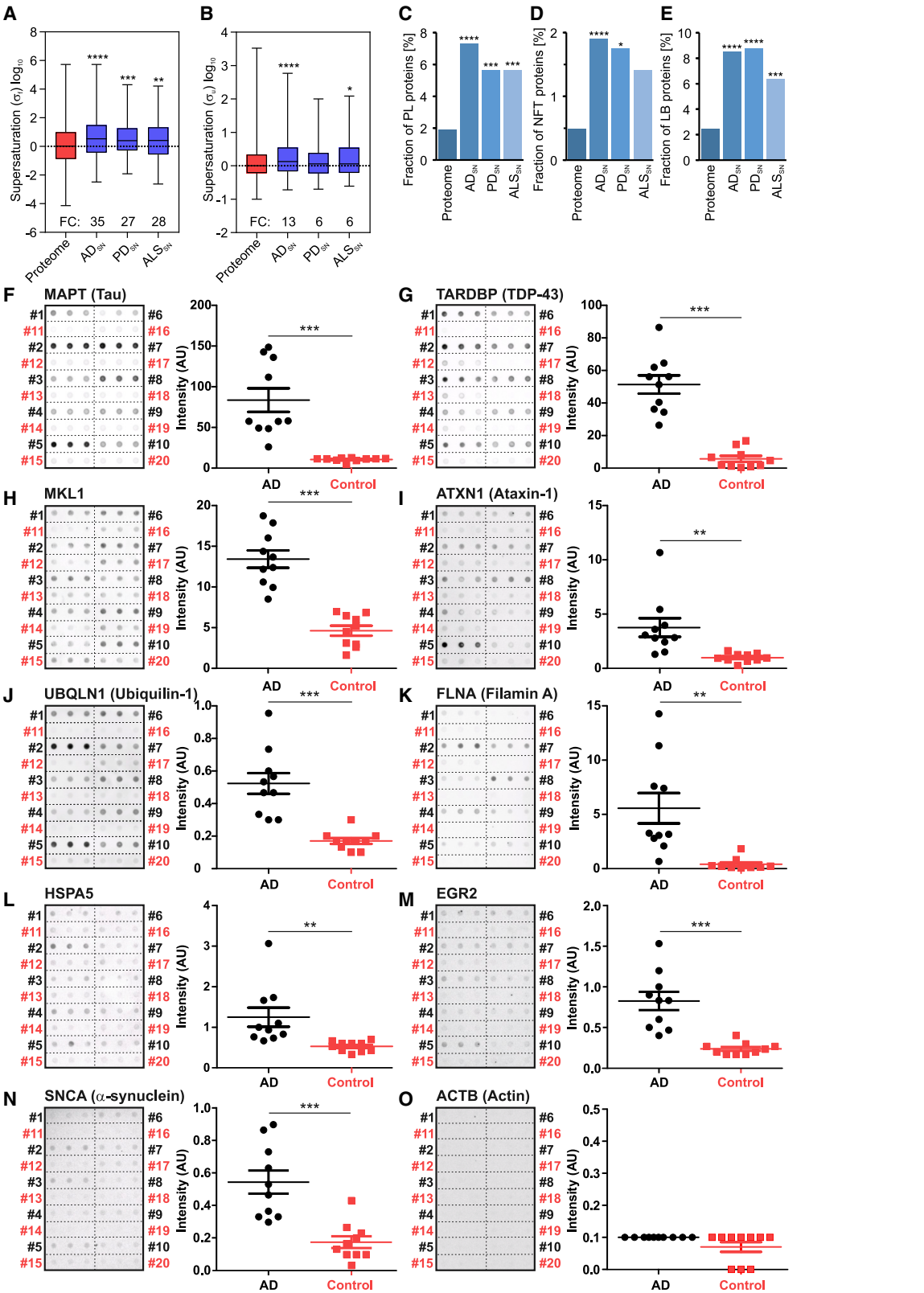

(legend on next page)

neurons (Kaneda et al., 2018). Many connections to known NDCPs were also observed for the guanine nucleotide exchange protein ARF-GEP$_{100}$ (*IQSEC1*) (Figures 4E and 4F), which regulates vesicle formation and phagocytosis in mammalian cells (Someya et al., 2010).

ND-Associated Subnetworks Contain Proteins that Aggregate in Patient Brains

Supersaturated proteins are metastable and have an elevated aggregation propensity in mammalian cells (Ciryam et al., 2013). Human proteins were previously classified according to their supersaturation scores σ_f and σ_u that measure the risk of folded (σ_f) and unfolded (σ_u) proteins to form insoluble aggregates. Using these scores, aggregation-prone proteins were predicted to be overrepresented among ND-associated proteins (Ciryam et al., 2015), suggesting that such proteins might also be enriched in disease subnetworks (Figure S4B; Table S5). We first calculated the median σ_u and σ_f supersaturation scores for the proteins in AD$_{SN}$, PD$_{SN}$, and ALS$_{SN}$ (Table S5) and then compared these values to the median score of the proteome. We found that the σ_f scores for the network proteins were significantly higher than those for the control proteins (Figure 5A), indicating that aggregation-prone proteins are enriched in the predicted subnetworks. The analysis of median σ_u scores revealed that unfolded proteins with a high aggregation propensity are less abundant in disease subnetworks, except for AD$_{SN}$ (Figure 5B), which contains many proteins with high σ_u scores.

Next, we assessed whether proteins that form abnormal aggregates in brains of patients with NDs tend to appear in the ND-associated subnetworks. We evaluated published proteomic studies and assessed whether proteins found in amyloid plaques (Liao et al., 2004), neurofibrillary tangles (NFTs) (Wang et al., 2005) or Lewy bodies (Xia et al., 2008) are present in the computationally predicted disease networks. We found that 117 (15.4%; hypergeometric $p < 0.0001$) of the 762 aggregated proteins in AD and PD patient brains are present in the predicted disease subnetworks (Figures 5C–5E), supporting our hypothesis that aggregation-prone proteins are enriched among ND-associated proteins.

Predicted ND Protein Modules Facilitate Identification of Aggregated Proteins in AD Patient Brains

To investigate whether proteins in AD$_{MO}$ (Figure 4D) are abnormally aggregated in disease, we analyzed postmortem brains of AD patients and age-matched controls using a filter retardation assay (FRA) (Wanker et al., 1999). We initially selected 15 proteins from AD$_{MO}$ for this analysis. Because of a lack of specific antibodies, however (Table S6), we finally assessed the aggregation state of 7 proteins in AD patient and control brains (Figures 5H–5N and S5A). For benchmarking, we first examined tau and TDP-43, which are aberrantly aggregated in AD brains (Krüger and Mandelkow, 2016; Wilson et al., 2011). Analysis of tissue homogenates (10 each, temporal cortex) with FRAs revealed significantly higher levels of tau and TDP-43 aggregates in AD samples than in controls (Figures 5F and 5G). Next, we analyzed the aggregation state of the predicted proteins ATXN1, filamin A (FLNA), ubiquilin-1 (UBQLN1), Hsp70 (HSPA5), ERG2, SNCA, and MKL1 in brain homogenates using the FRA. Except for SNCA (Kelley et al., 2018; Xu et al., 2002), all selected proteins had previously not been described to form abnormal aggregates in AD patient brains, whereas colocalization of UBQLN1 and FLNA with tau aggregates was reported (Feuillette et al., 2010; Mizukami et al., 2014). Strikingly, we found that all proteins were significantly more strongly aggregated in AD than in control brains (Figures 5H–5N), substantiating our hypothesis that aggregation-prone proteins are associated with NDs. The specificity of the applied antibodies was confirmed by SDS-PAGE and immunoblotting (Figure S5A). No aggregation was detected with the control protein actin (Figure 5O). Finally, we confirmed that high-molecular-weight MKL1, ATXN1, UBQLN1, and FLNA aggregates can also be detected in AD patient brains by native PAGE and immunoblotting (Figures S5B–S5E).

ARF-GEP$_{100}$ Controls Misfolding and Aggregation of Multiple NDCPs

Many well-known NDCPs such as SNCA and TDP-43 have a high propensity to self-assemble into insoluble protein aggregates in NDs (Sami et al., 2017). We hypothesized that NDCP-interacting proteins might control their aggregation propensity in disease-relevant model systems. To address this question, we focused on the protein ARF-GEP$_{100}$ (*IQSEC1*) that interacts with multiple aggregation-prone proteins such as TDP-43 and SOD1 (Figures 4E and 4F; Table S5) in yeast and LuTHy assays (Figure S6A). ARF-GEP$_{100}$ is expressed in brain and was previously shown to regulate phagocytosis (Someya et al., 2010), suggesting that it might influence the degradation of different misfolded NDCPs in mammalian cells.

We first assessed whether RNAi-mediated knockdown of the gene *M02B7.5* (*IQSEC1*) in a *C. elegans* model influences

Figure 5. Computationally Predicted Proteins Are Abnormally Aggregated in Postmortem Brains of AD Patients

(A and B) Comparison of supersaturation scores σ_f (A) and σ_u (B) of proteins in the proteome and proteins in the predicted ND-specific subnetworks. Boxplots extend from the lower to the upper quartiles, with the internal lines referring to the median values. The statistical significance was assessed by the Mann-Whitney U test with Bonferroni-corrected p values (*$p < 0.05$, **$p < 0.01$, ***$p < 0.001$, ****$p < 0.0001$). FC, fold change; the values indicate supersaturation scores above the median for the human proteome.

(C–E) Abundance of proteins found in aggregates of ND patient brains in ND-specific subnetworks and the whole proteome. (C) Proteins found in AD plaques, (D) proteins associated with NFTs, and (E) proteins identified in Lewy bodies. The statistical significance was assessed with a Fisher's exact test with Holm-Bonferroni corrections (*$p < 0.05$, ***$p < 0.001$, ****$p < 0.0001$). PL, plaques; LB, Lewy bodies.

(F–O) Detection of insoluble protein aggregates in postmortem brain homogenates of 10 AD patients (1–10, black lettering) and 10 age-matched controls (11–20, red lettering) using a native FRA. Triplicates per sample were filtered. Quantification of protein aggregates retained on filter membranes was performed using Aida image analysis software. The statistical significance was assessed with an unpaired, two-tailed t test (***$p < 0.001$, **$p < 0.01$). All data are expressed as mean ± SEM.

See also Tables S5 and S6 and Figures S4B–S4D and S5.

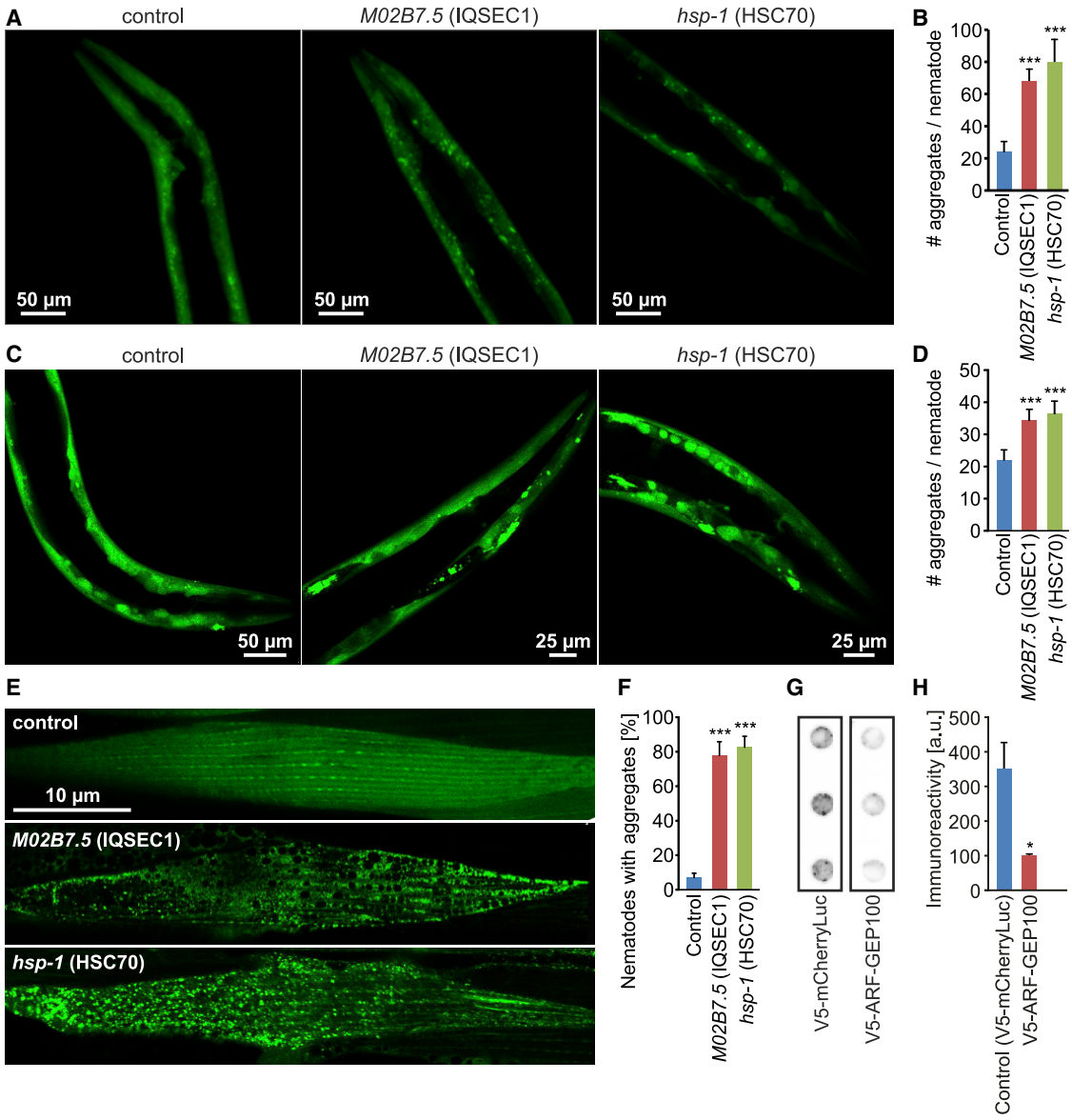

Figure 6. ARF-GEP$_{100}$ Influences Misfolding of Different Aggregation-Prone Polypeptides in Model Systems

(A) SYN-YFP aggregation phenotype resulting from RNAi-mediated knockdown of target genes in a transgenic *C. elegans* model. Representative images are shown.

(B) Quantification of aggregates (green dots) shown in (A). n = 7–10 nematodes per knockdown experiment were analyzed. ***$p < 0.001$ by two-sided t test.

(C) Q35-YFP aggregation phenotype resulting from RNAi-mediated knockdown of target genes in a transgenic *C. elegans* model. Representative images are shown.

(D) Quantification of aggregates (green dots) shown in (C). n = 20 nematodes per knockdown experiment were analyzed. ***$p < 0.001$ by two-sided t test.

(E) Luciferase-R188Q-R216Q-YFP aggregation phenotype resulting from RNAi-mediated knockdown of target genes in a transgenic *C. elegans* model. Representative images are shown.

(F) Quantification of aggregates (green dots) shown in (E). n = 20 worms per knockdown experiment were analyzed. ***$p < 0.001$ by two-sided t test.

(G) Effect of V5-tagged ARF-GEP$_{100}$ coproduction on CFP-HTTex1Q49 aggregation in HeLa cells. Representative images of mutant HTT aggregates retained on filter membranes (black dots) are shown.

(H) Quantification of results shown in (G). *$p < 0.05$ by two-sided t test.

Data in (B), (D), (F), and (H) are expressed as mean ± SEM.

See also Table S4 and Figures S3C–S3E and S6B–S6D.

α-synuclein-YFP (SYN-YFP) aggregation in muscle cells. In addition, the knockdown of the *hsp-1* gene, encoding the molecular chaperone Hsc70 (Nollen et al., 2004), was assessed as a positive control. We observed a strong increase of SYN-YFP aggregation upon knockdown of both genes (Figures 6A and 6B), suggesting that ARF-GEP$_{100}$, similar to Hsc70, controls

misfolding and aggregation of SNCA in nematodes. The RNAi-mediated knockdown of *IQSEC1* transcripts in SYN-YFP-expressing worms was confirmed in two independent qRT-PCR experiments (Figures S3D and S3E).

Next, we assessed whether knockdown of *M02B7.5* also influences polyQ-mediated protein aggregation (Scherzinger et al., 1999) in worms. Expression of Q35-YFP in *C. elegans* leads to the formation of proteotoxic aggregates in muscle cells, which increase in their abundance upon RNAi-mediated knockdown of *hsp-1* (Morley et al., 2002; Nollen et al., 2004). We observed that Q35-YFP aggregation was significantly increased in muscle cells when *M02B7.5* was knocked down (Figures 6C and 6D), indicating that ARF-GEP$_{100}$, similar to molecular chaperones (Mogk and Bukau, 2017), influences aggregation of different disease proteins in cells.

We also assessed whether knockdown of ARF-GEP$_{100}$ influences aggregation of the folding sensor luciferase-R188Q-R216Q-YFP (Rampelt et al., 2012) in worms. We found that this protein is soluble in muscle cells under control conditions. However, it formed insoluble protein aggregates when the genes *M02B7.5* and *hsp-1* were knocked down (Figures 6E and 6F).

Finally, we investigated whether overproduction of ARF-GEP$_{100}$ influences polyQ-mediated protein aggregation in mammalian cells. We coexpressed ARF-GEP$_{100}$ with a CFP-tagged HTTex1Q49 fusion protein in HeLa cells and quantified the formation of polyQ-containing protein aggregates after 24 h by FRA (Wanker et al., 1999). In a control experiment, the influence of mCherryLuc on CFP-HTTex1Q49 aggregation was assessed. We found ARF-GEP$_{100}$ overproduction significantly decreased the abundance of CFP-HTTex1Q49 aggregates in mammalian cells (Figures 6G and 6H). The expression of tagged recombinant proteins was confirmed by SDS-PAGE and immunoblotting (Figures S6B–S6D).

DISCUSSION

Screening for PPIs and integrating publicly available interaction data, we generated an interactome network (termed NN1.0ext) focused on proteins associated with various NDs, such as AD, PD, and ALS. It directly connects 4,956 human proteins via 30,374 candidate interactions, providing a framework for computational network-based interrogations (Barabási et al., 2011) and more focused, hypothesis-driven experiments (Arumughan et al., 2016).

In NN1.0ext, 1,348 partner proteins are linked to 94 well-known NDCPs, such as TDP-43, SNCA, LRRK2, and HTT, indicating that it contains relevant information for multiple NDs. Focused interaction maps centered on specific proteins can be extracted from the PPI data for more detailed functional annotation of disease proteins. NN1.0ext also highlights connections among NDCPs (Figure S2C), indicating that multiple relationships exist among ND-associated molecules. For example, we confirmed an interaction between the HD-causing protein HTT and optineurin (*OPTN*), which is mutated in ALS (Maruyama et al., 2010). Optineurin controls autophagy in mammalian cells (Ying and Yue, 2016), and mutations in this protein are linked to the accumulation of abnormal protein aggregates in brains of ALS patients (Maruyama et al., 2010). Our results implicate optineurin in HD and other NDs (Figure S2C), supporting previous evidence that it is a multifunctional adaptor with a role in different NDs (Markovinovic et al., 2017).

A disease phenotype is rarely the consequence of an abnormality in a single gene or protein but rather reflects a multitude of pathobiological processes connected in a complex network (Barabási et al., 2011). Starting from known NDCPs and the NN1.0ext PPI dataset, we computationally predicted subnetworks and interconnected protein modules for AD, PD and ALS (Figures 4D–4F), which contain many proteins that had not previously been linked to a specific disease. We propose that disease-causing missense mutations in NDCPs perturb a considerable number of disease-associated interactions, leading to neuronal dysfunction and neurotoxicity. Previous investigations indicate that missense mutations often change PPIs, suggesting that specific interaction perturbations underlie distinct ND phenotypes (Sahni et al., 2015).

We found that the predicted disease protein modules, e.g., PD$_{MO}$ and ALS$_{MO}$, contain distinct interactions (Figures 4E and 4F), indicating that specific molecular deficits and perturbations are the origin of a particular disease phenotype. However, we also found overlapping PPIs present in more than one of the modules, suggesting therapeutic strategies might be relevant for more than one ND (Ehrnhoefer et al., 2011). This is supported by our cross-comparisons, indicating that genetic modifiers (Chen and Burgoyne, 2012; Na et al., 2013) are linked to different NDCPs in our computationally predicted disease subnetworks (Figures 4A–4C). Our analysis also revealed that many other known human disease proteins (ODAPs) are linked to NDCPs (Figures 4G and 4H), suggesting that knowledge from other disease areas might stimulate ND-specific research. For example, the transcriptional coactivator MKL1 involved in cancer development is linked to many known NDCPs in the predicted modules (Figures 4D–4F). In the brain, however, MKL1 function is critical for dendritic spine maturation (Kaneda et al., 2018). A loss of this function in AD brains, e.g., through abnormal aggregation (Figure 5H), may contribute to disease development and progression.

A large body of previous evidence points to abnormal aggregation of NDCPs such as HTT, SNCA, tau, and TDP-43 as potential drivers of pathogenesis in NDs (Sami et al., 2017). Theoretical investigations indicate that various aggregation-prone proteins may be associated with NDs (Ciryam et al., 2015), suggesting that protein aggregation is a more widespread phenomenon than commonly appreciated. However, systematic experimental studies with biosamples from ND patients to support these considerations have been lacking. Here, we present experimental evidence that various computationally predicted AD-associated proteins, such as UBQLN1, FLNA, ATXN1, HSPA5, ERG2, SNCA, and MKL1, are aberrantly aggregated in AD patient brains (Figures 5H–5N), confirming that current assumptions underestimate the relevance of the phenomenon. We hypothesize that the initial formation of primary amyloid such as β-amyloid or tau may trigger an aggregation cascade that over time involves multiple proteins (Gidalevitz et al., 2006) and leads to synergistic dysfunction and toxicity in patient brains. However, different aggregation-prone proteins may precipitate independently, leading to the accumulation of spatially distinct protein deposits in

mammalian cells. The coexistence of TDP-43, tau, and SNCA aggregates in brains of AD patients has been described (Higashi et al., 2007), whereas abnormal aggregation of ATXN1 in AD brains has not been reported. Strikingly, loss of this protein was shown to potentiate AD pathogenesis in mouse brains (Suh et al., 2019), supporting our hypothesis that ATXN1 aggregation may contribute to AD pathogenesis. Mixed protein pathologies have been shown to be associated with more severe symptoms in AD patients (James et al., 2016) and PD patients (Irwin et al., 2013). A better understanding of the relationships between aggregate pathologies and their associated clinical phenotypes will be critical to clarifying the role of amyloidogenic protein aggregates in disease.

Our strategy to create a PPI map for proteins involved in NDs and to define potentially disease-relevant subnetworks and protein modules will extend our current understanding of ND mechanisms, like the identification of ARF-GEP$_{100}$ as a generic modulator of protein aggregation in mammalian cells and various disease models (Figure 6). However, it is important that the presented PPI network map of NDs be regarded as neither complete nor final. Many highly relevant disease proteins, like glucocerebrosidase (GBA) and various Rab proteins (e.g., RAB7-L1), have not been systematically screened, because cDNAs were not available or they acted as autoactivators in the Y2H assays. Further mapping, validation, and data integration efforts will create an even more comprehensive PPI dataset for proteins associated with NDs. To aid these efforts, NN1.0ext is a valuable resource that contains unique information for detecting disease modifiers, novel drug targets, and biomarkers for multiple NDs.

STAR★METHODS

Detailed methods are provided in the online version of this paper and include the following:

- KEY RESOURCES TABLE
- RESOURCE AVAILABILITY
  - Lead Contact
  - Materials Availability
  - Data and Code Availability
- EXPERIMENTAL MODEL AND SUBJECT DETAILS
  - Cells, *C. elegans* and *D. melanogaster* models
- METHOD DETAILS
  - Selection of ND-related target genes
  - Literature review for selected target genes
  - Enrichment analysis
  - Prediction of disease-relevant proteins
  - Construction of ND subnetworks and modules
  - Data cross-comparisons
  - Supersaturated, aggregation-prone proteins
  - Automated Y2H interaction screening
  - PPI detection in cells using DULIP and LuTHy
  - Selection of predicted AD-associated proteins
  - Selection of predicted TDP-43 modulators
  - Knockdown of target genes in *D. melanogaster*
  - Knockdown of target genes in *C. elegans*
  - Analysis of retina degeneration in flies
  - Protein aggregates in patient brains
  - Knockdown of MO2B7.5 (IQSEC1) in *C. elegans*
  - qRT-PCR with RNAi treated *C. elegans* strains
  - Co-transfection of HeLa cells
- QUANTIFICATION AND STATISTICAL ANALYSIS

SUPPLEMENTAL INFORMATION

Supplemental Information can be found online at https://doi.org/10.1016/j.celrep.2020.108050.

ACKNOWLEDGMENTS

We thank P. Trepte, K. Rau, K. Muehlenberg, S. Koeppen, R. Foulle, S. Plassmann, R. Kalis, N. Neuendorf, D. Rotte, and R. Friedrich for technical assistance. Furthermore, we thank E. Blanc for providing assistance in data analysis and M. Peters for critical discussion of the manuscript. This work was supported by grants from the German Research Foundation (SFB618, SFB740, Neurocure), the Federal Ministry of Education and Research (NGFN-Plus: NeuroNet, MooDS, Mutanom, Interaktom, Integrament), the European Union (EuroSpin and SynSys), and the Helmholtz Association (MSBN and HelMA) to E.E.W. The relevant grant numbers are SFB618, 618/3-09 SP A05; SFB740, 740/2-11; NeuroCure, EXC257; NeuroNet, 01GS08170; MooDS, 01GS08150; Mutanom, 01GS08108; Interaktom, 01GS0844; Integrament, 01ZX1314C; EuroSpin, Health-F2-2009-241498; SynSys, HEALTH-F2-2009-242167; MSBN, NW2; and HelMA, HA-215. R.S. and E.E.W. were supported by grant 3-12056 from the Helmholtz-Israel Cooperation in Personalized Medicine. Human brain samples for this study were provided by the Newcastle Brain Tissue Resource, which is partly funded by a grant from the UK Medical Research Council (G0400074), by NIHR Newcastle Biomedical Research Centre awarded to the Newcastle upon Tyne NHS Foundation Trust and Newcastle University, and as part of the Brains for Dementia Research Programme jointly funded by Alzheimer's Research UK and Alzheimer's Society.

AUTHOR CONTRIBUTIONS

A.K.T., J.R., S.-P.R., A.B., M.C., L.B., M.S., B.D.F., S.J., M.Z., K.A., L.P., and J.K. performed the experiments. C.H., A.B., N.A., A.M., J.R., S.-P.R., M.H.S., J.-F.F., M.A.A.-N., K.A., J.K., P.P., and R.S. analyzed the data and designed specific experiments. B.D.F., J.P.T., P.H., J.K., and R.S. provided vital reagents and technologies. The manuscript was written by E.E.W. with support from J.R., S-P.R., J.-F.F., C.H., S.S., and R.S. E.E.W. acquired the funding and provided overall supervision.

DECLARATION OF INTERESTS

The authors declare no competing interests.

Received: April 5, 2019
Revised: February 15, 2020
Accepted: July 28, 2020
Published: August 18, 2020

REFERENCES

Alanis-Lobato, G., Andrade-Navarro, M.A., and Schaefer, M.H. (2017). HIPPIE v2.0: enhancing meaningfulness and reliability of protein-protein interaction networks. Nucleic Acids Res. *45* (*D1*), D408–D414.

Amberger, J.S., Bocchini, C.A., Schiettecatte, F., Scott, A.F., and Hamosh, A. (2015). OMIM.org: Online Mendelian Inheritance in Man (OMIM®), an online catalog of human genes and genetic disorders. Nucleic Acids Res. *43*, D789–D798.

Archbold, H.C., Jackson, K.L., Arora, A., Weskamp, K., Tank, E.M., Li, X., Miguez, R., Dayton, R.D., Tamir, S., Klein, R.L., and Barmada, S.J. (2018). TDP43 nuclear export and neurodegeneration in models of amyotrophic lateral sclerosis and frontotemporal dementia. Sci. Rep. *8*, 4606.

Arumughan, A., Roske, Y., Barth, C., Forero, L.L., Bravo-Rodriguez, K., Redel, A., Kostova, S., McShane, E., Opitz, R., Faelber, K., et al. (2016). Quantitative interaction mapping reveals an extended UBX domain in ASPL that disrupts functional p97 hexamers. Nat. Commun. *7*, 13047.

Assenov, Y., Ramirez, F., Schelhorn, S.E., Lengauer, T., and Albrecht, M. (2008). Computing topological parameters of biological networks. Bioinformatics *24*, 282–284.

Bando, Y., Onuki, R., Katayama, T., Manabe, T., Kudo, T., Taira, K., and Tohyama, M. (2005). Double-strand RNA dependent protein kinase (PKR) is involved in the extrastriatal degeneration in Parkinson's disease and Huntington's disease. Neurochem. Int. *46*, 11–18.

Barabási, A.L., Gulbahce, N., and Loscalzo, J. (2011). Network medicine: a network-based approach to human disease. Nat. Rev. Genet. *12*, 56–68.

Bawa, P., Pradeep, P., Kumar, P., Choonara, Y.E., Modi, G., and Pillay, V. (2016). Multi-target therapeutics for neuropsychiatric and neurodegenerative disorders. Drug Discov. Today *21*, 1886–1914.

Braun, P., Tasan, M., Dreze, M., Barrios-Rodiles, M., Lemmens, I., Yu, H., Sahalie, J.M., Murray, R.R., Roncari, L., de Smet, A.S., et al. (2009). An experimentally derived confidence score for binary protein-protein interactions. Nat. Methods *6*, 91–97.

Brehme, M., Voisine, C., Rolland, T., Wachi, S., Soper, J.H., Zhu, Y., Orton, K., Villella, A., Garza, D., Vidal, M., et al. (2014). A chaperome subnetwork safeguards proteostasis in aging and neurodegenerative disease. Cell Rep. *9*, 1135–1150.

Brettschneider, J., Del Tredici, K., Lee, V.M., and Trojanowski, J.Q. (2015). Spreading of pathology in neurodegenerative diseases: a focus on human studies. Nat. Rev. Neurosci. *16*, 109–120.

Chaurasia, G., Iqbal, Y., Haenig, C., Herzel, H., Wanker, E.E., and Futschik, M.E. (2007). UniHI: an entry gate to the human protein interactome. Nucleic Acids Res. *35*, D590–D594.

Chen, X., and Burgoyne, R.D. (2012). Identification of common genetic modifiers of neurodegenerative diseases from an integrative analysis of diverse genetic screens in model organisms. BMC Genomics *13*, 71.

Chen-Plotkin, A.S., Lee, V.M., and Trojanowski, J.Q. (2010). TAR DNA-binding protein 43 in neurodegenerative disease. Nat. Rev. Neurol. *6*, 211–220.

Chiti, F., and Dobson, C.M. (2006). Protein misfolding, functional amyloid, and human disease. Annu. Rev. Biochem. *75*, 333–366.

Ciryam, P., Tartaglia, G.G., Morimoto, R.I., Dobson, C.M., and Vendruscolo, M. (2013). Widespread aggregation and neurodegenerative diseases are associated with supersaturated proteins. Cell Rep. *5*, 781–790.

Ciryam, P., Kundra, R., Morimoto, R.I., Dobson, C.M., and Vendruscolo, M. (2015). Supersaturation is a major driving force for protein aggregation in neurodegenerative diseases. Trends Pharmacol. Sci. *36*, 72–77.

Conforti, F.L., Spataro, R., Sproviero, W., Mazzei, R., Cavalcanti, F., Condino, F., Simone, I.L., Logroscino, G., Patitucci, A., Magariello, A., et al. (2012). Ataxin-1 and ataxin-2 intermediate-length PolyQ expansions in amyotrophic lateral sclerosis. Neurology *79*, 2315–2320.

Cowen, L., Ideker, T., Raphael, B.J., and Sharan, R. (2017). Network propagation: a universal amplifier of genetic associations. Nat. Rev. Genet. *18*, 551–562.

Dietzl, G., Chen, D., Schnorrer, F., Su, K.C., Barinova, Y., Fellner, M., Gasser, B., Kinsey, K., Oppel, S., Scheiblauer, S., et al. (2007). A genome-wide transgenic RNAi library for conditional gene inactivation in Drosophila. Nature *448*, 151–156.

Donato, S.D., Mariotti, C., and Taroni, F. (2012). Spinocerebellar ataxia type 1. Handb. Clin. Neurol. *103*, 399–421.

Ehrnhoefer, D.E., Wong, B.K., and Hayden, M.R. (2011). Convergent pathogenic pathways in Alzheimer's and Huntington's diseases: shared targets for drug development. Nat. Rev. Drug Discov. *10*, 853–867.

Elion, E.A. (2006). Detection of protein-protein interactions by coprecipitation. Curr. Protoc. Mol. Biol. *76*, 20.5.1–20.5.10.

Feuillette, S., Deramecourt, V., Laquerriere, A., Duyckaerts, C., Delisle, M.B., Maurage, C.A., Blum, D., Buée, L., Frébourg, T., Campion, D., and Lecourtois, M. (2010). Filamin-A and Myosin VI colocalize with fibrillary Tau protein in Alzheimer's disease and FTDP-17 brains. Brain Res. *1345*, 182–189.

Fontaine, J.F., Barbosa-Silva, A., Schaefer, M., Huska, M.R., Muro, E.M., and Andrade-Navarro, M.A. (2009). MedlineRanker: flexible ranking of biomedical literature. Nucleic Acids Res. *37*, W141–W146.

Fontaine, J.F., Priller, F., Barbosa-Silva, A., and Andrade-Navarro, M.A. (2011). Génie: literature-based gene prioritization at multi genomic scale. Nucleic Acids Res. *39*, W455–W461.

Freibaum, B.D., Chitta, R.K., High, A.A., and Taylor, J.P. (2010). Global analysis of TDP-43 interacting proteins reveals strong association with RNA splicing and translation machinery. J. Proteome Res. *9*, 1104–1120.

Gatchel, J.R., and Zoghbi, H.Y. (2005). Diseases of unstable repeat expansion: mechanisms and common principles. Nat. Rev. Genet. *6*, 743–755.

Gidalevitz, T., Ben-Zvi, A., Ho, K.H., Brignull, H.R., and Morimoto, R.I. (2006). Progressive disruption of cellular protein folding in models of polyglutamine diseases. Science *311*, 1471–1474.

Goedert, M. (2015). NEURODEGENERATION. Alzheimer's and Parkinson's diseases: The prion concept in relation to assembled Aβ, tau, and α-synuclein. Science *349*, 1255555.

Goehler, H., Lalowski, M., Stelzl, U., Waelter, S., Stroedicke, M., Worm, U., Droege, A., Lindenberg, K.S., Knoblich, M., Haenig, C., et al. (2004). A protein interaction network links GIT1, an enhancer of huntingtin aggregation, to Huntington's disease. Mol. Cell *15*, 853–865.

Gottlieb, A., Magger, O., Berman, I., Ruppin, E., and Sharan, R. (2011). PRINCIPLE: a tool for associating genes with diseases via network propagation. Bioinformatics *27*, 3325–3326.

Gratuze, M., Cisbani, G., Cicchetti, F., and Planel, E. (2016). Is Huntington's disease a tauopathy? Brain *139*, 1014–1025.

Grünberg, R., Burnier, J.V., Ferrar, T., Beltran-Sastre, V., Stricher, F., Van Der Sloot, A.M., Garcia-Olivas, R., Mallabiabarrena, A., Sanjuan, X., Zimmermann, T., et al. (2013). Engineering of weak helper interactions for high-efficiency FRET probes. Nat. Methods *10*, 1021–1027.

Hein, M.Y., Hubner, N.C., Poser, I., Cox, J., Nagaraj, N., Toyoda, Y., Gak, I.A., Weisswange, I., Mansfeld, J., Buchholz, F., et al. (2015). A human interactome in three quantitative dimensions organized by stoichiometries and abundances. Cell *163*, 712–723.

Higashi, S., Iseki, E., Yamamoto, R., Minegishi, M., Hino, H., Fujisawa, K., Togo, T., Katsuse, O., Uchikado, H., Furukawa, Y., et al. (2007). Concurrence of TDP-43, tau and alpha-synuclein pathology in brains of Alzheimer's disease and dementia with Lewy bodies. Brain Res. *1184*, 284–294.

Hornbeck, P.V., Zhang, B., Murray, B., Kornhauser, J.M., Latham, V., and Skrzypek, E. (2015). PhosphoSitePlus, 2014: mutations, PTMs and recalibrations. Nucleic Acids Res. *43*, D512–D520.

Hosp, F., Vossfeldt, H., Heinig, M., Vasiljevic, D., Arumughan, A., Wyler, E., Landthaler, M., Hubner, N., Wanker, E.E., Lannfelt, L., et al.; Genetic and Environmental Risk for Alzheimer's Disease GERAD1 Consortium (2015). Quantitative interaction proteomics of neurodegenerative disease proteins. Cell Rep. *11*, 1134–1146.

Hugon, J., Mouton-Liger, F., Dumurgier, J., and Paquet, C. (2017). PKR involvement in Alzheimer's disease. Alzheimers Res. Ther. *9*, 83.

Irwin, D.J., Lee, V.M., and Trojanowski, J.Q. (2013). Parkinson's disease dementia: convergence of α-synuclein, tau and amyloid-β pathologies. Nat. Rev. Neurosci. *14*, 626–636.

James, B.D., Wilson, R.S., Boyle, P.A., Trojanowski, J.Q., Bennett, D.A., and Schneider, J.A. (2016). TDP-43 stage, mixed pathologies, and clinical Alzheimer's-type dementia. Brain *139*, 2983–2993.

Jellinger, K.A. (2012). Interaction between pathogenic proteins in neurodegenerative disorders. J. Cell. Mol. Med. *16*, 1166–1183.

Kaltenbach, L.S., Romero, E., Becklin, R.R., Chettier, R., Bell, R., Phansalkar, A., Strand, A., Torcassi, C., Savage, J., Hurlburt, A., et al. (2007). Huntingtin

interacting proteins are genetic modifiers of neurodegeneration. PLoS Genet. *3*, e82.

Kamath, R.S., Fraser, A.G., Dong, Y., Poulin, G., Durbin, R., Gotta, M., Kanapin, A., Le Bot, N., Moreno, S., Sohrmann, M., et al. (2003). Systematic functional analysis of the Caenorhabditis elegans genome using RNAi. Nature *421* (*6920*), 231–237.

Kaneda, M., Sakagami, H., Hida, Y., Ohtsuka, T., Satou, N., Ishibashi, Y., Fukuchi, M., Krysiak, A., Ishikawa, M., Ihara, D., et al. (2018). Synaptic localisation of SRF coactivators, MKL1 and MKL2, and their role in dendritic spine morphology. Sci. Rep. *8*, 727.

Keiser, M.S., Kordasiewicz, H.B., and McBride, J.L. (2016). Gene suppression strategies for dominantly inherited neurodegenerative diseases: lessons from Huntington's disease and spinocerebellar ataxia. Hum. Mol. Genet. *25* (*R1*), R53–R64.

Kelley, A.R., Colley, M.E., Perry, G., and Bach, S.B.H. (2018). Incubation with Cu(II) and Zn(II) salts enhances MALDI-TOF mass spectra of amyloid-beta and α-synuclein toward in vivo analysis. J. Mass Spectrom. *53*, 162–171.

Khanam, H., Ali, A., Asif, M., and Shamsuzzaman. (2016). Neurodegenerative diseases linked to misfolded proteins and their therapeutic approaches: A review. Eur. J. Med. Chem. *124*, 1121–1141.

Khurana, V., Peng, J., Chung, C.Y., Auluck, P.K., Fanning, S., Tardiff, D.F., Bartels, T., Koeva, M., Eichhorn, S.W., Benyamini, H., et al. (2017). Genome-Scale Networks Link Neurodegenerative Disease Genes to α-Synuclein through Specific Molecular Pathways. Cell Syst. *4*, 157–170.

Kirstein, J., Arnsburg, K., Scior, A., Szlachcic, A., Guilbride, D.L., Morimoto, R.I., Bukau, B., and Nillegoda, N.B. (2017). In vivo properties of the disaggregase function of J-proteins and Hsc70 in Caenorhabditis elegans stress and aging. Aging Cell *16*, 1414–1424.

Knöll, B., Kretz, O., Fiedler, C., Alberti, S., Schütz, G., Frotscher, M., and Nordheim, A. (2006). Serum response factor controls neuronal circuit assembly in the hippocampus. Nat. Neurosci. *9*, 195–204.

Krüger, L., and Mandelkow, E.M. (2016). Tau neurotoxicity and rescue in animal models of human Tauopathies. Curr. Opin. Neurobiol. *36*, 52–58.

Lamitina, T., Huang, C.G., and Strange, K. (2006). Genome-wide RNAi screening identifies protein damage as a regulator of osmoprotective gene expression. Proc. Natl. Acad. Sci. USA *103*, 12173–12178.

Liao, L., Cheng, D., Wang, J., Duong, D.M., Losik, T.G., Gearing, M., Rees, H.D., Lah, J.J., Levey, A.I., and Peng, J. (2004). Proteomic characterization of postmortem amyloid plaques isolated by laser capture microdissection. J. Biol. Chem. *279*, 37061–37068.

Lill, C.M. (2016). Genetics of Parkinson's disease. Mol. Cell. Probes *30*, 386–396.

Lim, J., Hao, T., Shaw, C., Patel, A.J., Szabó, G., Rual, J.F., Fisk, C.J., Li, N., Smolyar, A., Hill, D.E., et al. (2006). A protein-protein interaction network for human inherited ataxias and disorders of Purkinje cell degeneration. Cell *125*, 801–814.

Limviphuvadh, V., Tanaka, S., Goto, S., Ueda, K., and Kanehisa, M. (2007). The commonality of protein interaction networks determined in neurodegenerative disorders (NDDs). Bioinformatics *23*, 2129–2138.

Ling, S.C., Polymenidou, M., and Cleveland, D.W. (2013). Converging mechanisms in ALS and FTD: disrupted RNA and protein homeostasis. Neuron *79*, 416–438.

Lu, T., Pan, Y., Kao, S.Y., Li, C., Kohane, I., Chan, J., and Yankner, B.A. (2004). Gene regulation and DNA damage in the ageing human brain. Nature *429*, 883–891.

Markovinovic, A., Cimbro, R., Ljutic, T., Kriz, J., Rogelj, B., and Munitic, I. (2017). Optineurin in amyotrophic lateral sclerosis: Multifunctional adaptor protein at the crossroads of different neuroprotective mechanisms. Prog. Neurobiol. *154*, 1–20.

Maruyama, H., Morino, H., Ito, H., Izumi, Y., Kato, H., Watanabe, Y., Kinoshita, Y., Kamada, M., Nodera, H., Suzuki, H., et al. (2010). Mutations of optineurin in amyotrophic lateral sclerosis. Nature *465*, 223–226.

Mazza, A., Klockmeier, K., Wanker, E., and Sharan, R. (2016). An integer programming framework for inferring disease complexes from network data. Bioinformatics *32*, i271–i277.

Mizukami, K., Abrahamson, E.E., Mi, Z., Ishikawa, M., Watanabe, K., Kinoshita, S., Asada, T., and Ikonomovic, M.D. (2014). Immunohistochemical analysis of ubiquilin-1 in the human hippocampus: association with neurofibrillary tangle pathology. Neuropathology *34*, 11–18.

Mogk, A., and Bukau, B. (2017). Role of sHsps in organizing cytosolic protein aggregation and disaggregation. Cell Stress Chaperones *22*, 493–502.

Morley, J.F., Brignull, H.R., Weyers, J.J., and Morimoto, R.I. (2002). The threshold for polyglutamine-expansion protein aggregation and cellular toxicity is dynamic and influenced by aging in Caenorhabditis elegans. Proc. Natl. Acad. Sci. USA *99*, 10417–10422.

Na, D., Rouf, M., O'Kane, C.J., Rubinsztein, D.C., and Gsponer, J. (2013). NeuroGeM, a knowledgebase of genetic modifiers in neurodegenerative diseases. BMC Med. Genomics *6*, 52.

Nollen, E.A., Garcia, S.M., van Haaften, G., Kim, S., Chavez, A., Morimoto, R.I., and Plasterk, R.H. (2004). Genome-wide RNA interference screen identifies previously undescribed regulators of polyglutamine aggregation. Proc. Natl. Acad. Sci. USA *101*, 6403–6408.

Orchard, S., Ammari, M., Aranda, B., Breuza, L., Briganti, L., Broackes-Carter, F., Campbell, N.H., Chavali, G., Chen, C., del-Toro, N., et al. (2014). The MIntAct project–IntAct as a common curation platform for 11 molecular interaction databases. Nucleic Acids Res. *2014 Jan* (*42*), D358–D363.

Pechmann, S., Levy, E.D., Tartaglia, G.G., and Vendruscolo, M. (2009). Physicochemical principles that regulate the competition between functional and dysfunctional association of proteins. Proc. Natl. Acad. Sci. USA *106*, 10159–10164.

Pentony, M.M., and Jones, D.T. (2010). Modularity of intrinsic disorder in the human proteome. Proteins *78*, 212–221.

Perez-Iratxeta, C., Wjst, M., Bork, P., and Andrade, M.A. (2005). G2D: a tool for mining genes associated with disease. BMC Genet. *6*, 45.

Rampelt, H., Kirstein-Miles, J., Nillegoda, N.B., Chi, K., Scholz, S.R., Morimoto, R.I., and Bukau, B. (2012). Metazoan Hsp70 machines use Hsp110 to power protein disaggregation. EMBO J. *31*, 4221–4235.

Raychaudhuri, S., Dey, S., Bhattacharyya, N.P., and Mukhopadhyay, D. (2009). The role of intrinsically unstructured proteins in neurodegenerative diseases. PLoS ONE *4*, e5566.

Ritson, G.P., Custer, S.K., Freibaum, B.D., Guinto, J.B., Geffel, D., Moore, J., Tang, W., Winton, M.J., Neumann, M., Trojanowski, J.Q., et al. (2010). TDP-43 mediates degeneration in a novel Drosophila model of disease caused by mutations in VCP/p97. J. Neurosci. *30*, 7729–7739.

Rolland, T., Taşan, M., Charloteaux, B., Pevzner, S.J., Zhong, Q., Sahni, N., Yi, S., Lemmens, I., Fontanillo, C., Mosca, R., et al. (2014). A proteome-scale map of the human interactome network. Cell *159*, 1212–1226.

Rosenberg, R.N., Lambracht-Washington, D., Yu, G., and Xia, W. (2016). Genomics of Alzheimer Disease: A Review. JAMA Neurol. *73*, 867–874.

Ross, C.A., Aylward, E.H., Wild, E.J., Langbehn, D.R., Long, J.D., Warner, J.H., Scahill, R.I., Leavitt, B.R., Stout, J.C., Paulsen, J.S., et al. (2014). Huntington disease: natural history, biomarkers and prospects for therapeutics. Nat. Rev. Neurol. *10*, 204–216.

Rubinsztein, D.C. (2006). The roles of intracellular protein-degradation pathways in neurodegeneration. Nature *443*, 780–786.

Ruepp, A., Waegele, B., Lechner, M., Brauner, B., Dunger-Kaltenbach, I., Fobo, G., Frishman, G., Montrone, C., and Mewes, H.W. (2010). CORUM: the comprehensive resource of mammalian protein complexes—2009. Nucleic Acids Res. *38*, D497–D501.

Sahni, N., Yi, S., Taipale, M., Fuxman Bass, J.I., Coulombe-Huntington, J., Yang, F., Peng, J., Weile, J., Karras, G.I., Wang, Y., et al. (2015). Widespread macromolecular interaction perturbations in human genetic disorders. Cell *161*, 647–660.

Sami, N., Rahman, S., Kumar, V., Zaidi, S., Islam, A., Ali, S., Ahmad, F., and Hassan, M.I. (2017). Protein aggregation, misfolding and consequential human neurodegenerative diseases. Int. J. Neurosci. *127*, 1047–1057.

Scharenberg, M.A., Chiquet-Ehrismann, R., and Asparuhova, M.B. (2010). Megakaryoblastic leukemia protein-1 (MKL1): Increasing evidence for an involvement in cancer progression and metastasis. Int. J. Biochem. Cell Biol. *42*, 1911–1914.

Scherzinger, E., Sittler, A., Schweiger, K., Heiser, V., Lurz, R., Hasenbank, R., Bates, G.P., Lehrach, H., and Wanker, E.E. (1999). Self-assembly of polyglutamine-containing huntingtin fragments into amyloid-like fibrils: implications for Huntington's disease pathology. Proc. Natl. Acad. Sci. USA *96*, 4604–4609.

Shannon, P., Markiel, A., Ozier, O., Baliga, N.S., Wang, J.T., Ramage, D., Amin, N., Schwikowski, B., and Ideker, T. (2003). Cytoscape: a software environment for integrated models of biomolecular interaction networks. Genome Research *13*, 2498–2504.

Shimizu, K., and Toh, H. (2009). Interaction between intrinsically disordered proteins frequently occurs in a human protein-protein interaction network. J. Mol. Biol. *392*, 1253–1265.

Sigoillot, F.D., and King, R.W. (2011). Vigilance and validation: Keys to success in RNAi screening. ACS Chem. Biol. *6*, 47–60.

Someya, A., Moss, J., and Nagaoka, I. (2010). The guanine nucleotide exchange protein for ADP-ribosylation factor 6, ARF-GEP100/BRAG2, regulates phagocytosis of monocytic phagocytes in an ARF6-dependent process. J. Biol. Chem. *285*, 30698–30707.

Soto, C. (2012). Transmissible proteins: expanding the prion heresy. Cell *149*, 968–977.

Sreedharan, J., Blair, I.P., Tripathi, V.B., Hu, X., Vance, C., Rogelj, B., Ackerley, S., Durnall, J.C., Williams, K.L., Buratti, E., et al. (2008). TDP-43 mutations in familial and sporadic amyotrophic lateral sclerosis. Science *319*, 1668–1672.

Stelzl, U., Worm, U., Lalowski, M., Haenig, C., Brembeck, F.H., Goehler, H., Stroedicke, M., Zenkner, M., Schoenherr, A., Koeppen, S., et al. (2005). A human protein-protein interaction network: a resource for annotating the proteome. Cell *122*, 957–968.

Stroedicke, M., Bounab, Y., Strempel, N., Klockmeier, K., Yigit, S., Friedrich, R.P., Chaurasia, G., Li, S., Hesse, F., Riechers, S.P., et al. (2015). Systematic interaction network filtering identifies CRMP1 as a novel suppressor of huntingtin misfolding and neurotoxicity. Genome Res. *25*, 701–713.

Suh, J., Romano, D.M., Nitschke, L., Herrick, S.P., DiMarzio, B.A., Dzhala, V., Bae, J.S., Oram, M.K., Zheng, Y., Hooli, B., et al. (2019). Loss of Ataxin-1 Potentiates Alzheimer's Pathogenesis by Elevating Cerebral BACE1 Transcription. Cell *178*, 1159–1175.

Tartaglia, G.G., Pawar, A.P., Campioni, S., Dobson, C.M., Chiti, F., and Vendruscolo, M. (2008). Prediction of aggregation-prone regions in structured proteins. J. Mol. Biol. *380*, 425–436.

Taylor, J.P., Brown, R.H., Jr., and Cleveland, D.W. (2016). Decoding ALS: from genes to mechanism. Nature *539*, 197–206.

Thomas, S., and Bonchev, D. (2010). A survey of current software for network analysis in molecular biology. Hum. Genomics *4*, 353–360.

Toyoshima, Y., and Takahashi, H. (2014). TDP-43 pathology in polyglutamine diseases: with reference to amyotrphic lateral sclerosis. Neuropathology *34*, 77–82.

Trepte, P., Buntru, A., Klockmeier, K., Willmore, L., Arumughan, A., Secker, C., Zenkner, M., Brusendorf, L., Rau, K., Redel, A., and Wanker, E.E. (2015). DULIP: A Dual Luminescence-Based Co-Immunoprecipitation Assay for Interactome Mapping in Mammalian Cells. J. Mol. Biol. *427*, 3375–3388.

Trepte, P., Kruse, S., Kostova, S., Hoffmann, S., Buntru, A., Tempelmeier, A., Secker, C., Diez, L., Schulz, A., Klockmeier, K., et al. (2018). LuTHy: a double-readout bioluminescence-based two-hybrid technology for quantitative mapping of protein-protein interactions in mammalian cells. Mol. Syst. Biol. *14*, e8071.

Uversky, V.N., Oldfield, C.J., and Dunker, A.K. (2008). Intrinsically disordered proteins in human diseases: introducing the D2 concept. Annu. Rev. Biophys. *37*, 215–246.

Vanunu, O., Magger, O., Ruppin, E., Shlomi, T., and Sharan, R. (2010). Associating genes and protein complexes with disease via network propagation. PLoS Comput. Biol. *6*, e1000641.

Venkatesan, K., Rual, J.F., Vazquez, A., Stelzl, U., Lemmens, I., Hirozane-Kishikawa, T., Hao, T., Zenkner, M., Xin, X., Goh, K.I., et al. (2009). An empirical framework for binary interactome mapping. Nat. Methods *6*, 83–90.

Vinayagam, A., Stelzl, U., Foulle, R., Plassmann, S., Zenkner, M., Timm, J., Assmus, H.E., Andrade-Navarro, M.A., and Wanker, E.E. (2011). A directed protein interaction network for investigating intracellular signal transduction. Sci. Signal. *4*, rs8.

Wang, Q., Woltjer, R.L., Cimino, P.J., Pan, C., Montine, K.S., Zhang, J., and Montine, T.J. (2005). Proteomic analysis of neurofibrillary tangles in Alzheimer disease identifies GAPDH as a detergent-insoluble paired helical filament tau binding protein. FASEB J. *19*, 869–871.

Wanker, E.E., Rovira, C., Scherzinger, E., Hasenbank, R., Walter, S., Tait, D., Colicelli, J., and Lehrach, H. (1997). HIP-I: a huntingtin interacting protein isolated by the yeast two-hybrid system. Human Molecular Genetics *6*, 487–495.

Wanker, E.E., Scherzinger, E., Heiser, V., Sittler, A., Eickhoff, H., and Lehrach, H. (1999). Membrane filter assay for detection of amyloid-like polyglutamine-containing protein aggregates. Methods Enzymol. *309*, 375–386.

Wilson, A.C., Dugger, B.N., Dickson, D.W., and Wang, D.S. (2011). TDP-43 in aging and Alzheimer's disease—a review. Int. J. Clin. Exp. Pathol. *4*, 147–155.

Wishart, D.S. (2007). In silico drug exploration and discovery using DrugBank. Current protocols in bioinformatics *2007 Jun* (*Chapter 14*), Unit 14.4.

Wishart, D.S., Knox, C., Guo, A.C., Shrivastava, S., Hassanali, M., Stothard, P., Chang, Z., and Woolsey, J. (2006). DrugBank: a comprehensive resource for in silico drug discovery and exploration. Nucleic Acids Res. *34*, D668–D672.

Woodsmith, J., and Stelzl, U. (2014). Studying post-translational modifications with protein interaction networks. Curr. Opin. Struct. Biol. *24*, 34–44.

Xia, Q., Liao, L., Cheng, D., Duong, D.M., Gearing, M., Lah, J.J., Levey, A.I., and Peng, J. (2008). Proteomic identification of novel proteins associated with Lewy bodies. Front. Biosci. *13*, 3850–3856.

Xu, G., Gonzales, V., and Borchelt, D.R. (2002). Rapid detection of protein aggregates in the brains of Alzheimer patients and transgenic mouse models of amyloidosis. Alzheimer Dis. Assoc. Disord. *16*, 191–195.

Xu, W., Tan, L., and Yu, J.T. (2015). Link between the SNCA gene and parkinsonism. Neurobiol. Aging *36*, 1505–1518.

Ying, H., and Yue, B.Y. (2016). Optineurin: The autophagy connection. Exp. Eye Res. *144*, 73–80.

Zhang, C., Browne, A., Child, D., Divito, J.R., Stevenson, J.A., and Tanzi, R.E. (2010). Loss of function of ATXN1 increases amyloid beta-protein levels by potentiating beta-secretase processing of beta-amyloid precursor protein. J. Biol. Chem. *285*, 8515–8526.

STAR★METHODS

KEY RESOURCES TABLE

REAGENT or RESOURCE	SOURCE	IDENTIFIER
Antibodies		
Rabbit polyclonal anti-sheep IgG	Jackson ImmunoResearch Labs; Dianova	Cat#313-005-003; RRID:AB_2339937
Rabbit polyclonal anti-tau12 (tau 6-18)	BioLegend	Cat#806501; RRID:AB_2564707
Rabbit polyclonal anti-TDP-43	Proteintech Group	Cat#10782-2-AP; RRID:AB_615042
Rabbit polyclonal anti-ataxin-1	Cell Signaling Technology	Cat#2177; RRID:AB_2061047
Rabbit polyclonal anti-mouse IgG (Fc specific) POD	Sigma-Aldrich	Cat#A0168; RRID:AB_257867
Mouse monoclonal anti-α-tubulin	Sigma-Aldrich	Cat#T9026; RRID:AB_477593
Anti-α-Synuclein antibody, Mouse monoclonal	Sigma-Aldrich	Cat#S5566; RRID:AB_261518
Rabbit anti-MKL1 (C-Term)	Aviva systems biology; Antikörper online	Cat#ARP37504_T100; RRID:AB_842351
Rabbit anti-UBQLN1	Elabscience; Antikörper online	Cat#E-AB-14655; RRID:AB_2750981
Mouse monoclonal anti-beta Actin	Abcam	Cat#ab8224; RRID:AB_449644
Rabbit polyclonal anti-HSPA5	Antikörper online	Cat#ABIN651231; RRID: AB_10818618
Rabbit anti-EGR2	Abcam	Cat#ab108399; RRID:AB_10862073
Rabbit anti-FLNA (Filamin A)	Assay Biotech; Antikörper online	Cat#ABIN1532246; RRID:AB_10696433
Chemicals, Peptides, and Recombinant Proteins		
Isopropyl-β-D-thiogalactopyranosid (IPTG)	Sigma-Aldrich	CAS ID: 367-93-1
Levamisole	Sigma-Aldrich	CAS ID: 14769-73-4 (Levamisol)
DAPI	Sigma-Aldrich	CAS ID: 28718-90-3 (Dihydrochlorid)
Agarose	Sigma-Aldrich	Cat#16500500
LR clonase	Thermo Fisher Scientific	Cat#11791019
β-galactosidase enzyme	Sigma-Aldrich	Roche: 10745731001
High density nylon membranes	Thermo Fisher Scientific	Cat#77015
Opti-MEM® I Reduced Serum Medium	Thermo Fisher Scientific	Cat#31985062
Tween 20 (PBS-T)	Sigma-Aldrich	CAS ID: 9005-64-5
Protease inhibitor cocktail (Tm complete)	Sigma-Aldrich	Roche: 04693116001
Tris hydrochloride (Tris-HCl)	Sigma-Aldrich	Roche: 10812846001; CAS ID: 1185-53-1
SDS	Sigma-Aldrich	CAS ID: 151-21-3
Sodium deoxycholate	Sigma-Aldrich	CAS ID: 302-95-4
Triton X-100	Thermo Fisher Scientific	Cat#HFH10
Benzonase	Sigma-Aldrich	CAS ID: 9025-65-4
BSA protein	Thermo Fisher Scientific	Cat#AM2616
Cellulose acetate membrane	GE Healthcare Life Sciences	Product code/ID: 7000-0002
PBS buffer	GE Healthcare Life Sciences	Product code/ID: BR100672
Skim milk	Sigma-Aldrich	CAS ID: 999999-99-4
Dulbecco's modified Eagle's medium (DMEM)	Thermo Fisher Scientific	Cat#31885049
Fetal Bovine Serum (FBS)	Thermo Fisher Scientific	Cat#10270098
Penicillin-Streptomycin (P/S) antibiotic	Thermo Fisher Scientific	Cat#15140122
Linear Polyethyleneimine (PEI)	Polysciences	Cat#23966-1
HEPES buffer	Promega	Cat#H5302
NP-40	Sigma-Aldrich	CAS ID: 9016-45-9
Deoxycholate	Sigma-Aldrich	CAS ID: 302-95-4
Ethylenediaminetetraacetic acid (EDTA)	Sigma-Aldrich	CAS ID: 60-00-4

(*Continued on next page*)

Continued

REAGENT or RESOURCE	SOURCE	IDENTIFIER
Dithiothreitol (DTT)	Sigma-Aldrich	CAS ID: 3483-12-3
PMSF	Promega	Cat#G6521
Dual-Glo luciferase buffer	Promega	Cat#E298B-C
Dual-Glo Stop and Glo buffer	Promega	Cat#E314B-C
Bovine serum albumin	Sigma-Aldrich	Cat#9048-46-8
Nematode Growth Media (NGM)	Teknova	Cat#N1098
M9 medium	Sigma-Aldrich	Cat#M6030
Ampicillin	Sigma-Aldrich	CAS ID: 7177-48-2
X-Gal substrate	Thermo Fisher Scientific	Cat#B1690
Bouin's fixative	Sigma-Aldrich	Cat#HT10132
Critical Commercial Assays		
QIAprep 96 Turbo Miniprep Kit (4)	QIAGEN	Cat#27191
Pierce BCA protein assay kit	Thermo Fisher Scientific	Cat#23225
ChemiGlow West Chemilumineszenz Substrat Kit	Biozym	Cat#518020
Deposited Data		
UAS-RNAi lines	Vienna Drosophila Resource Center (VDRC)	RRID: SCR_013805 (http://stockcenter.vdrc.at/control/main)
UAS-RNAi lines	Bloomington Drosophila Stock Center (Indiana University, Bloomington, IN, USA)	RRID: SCR_006457 (https://bdsc.indiana.edu/)
PPIs from co-purified AP-LC-MS/MS data	Freibaum et al., 2010	N/A
Dataset of human genes and *C. elegans* orthologs	This paper and Ahringer library (Kamath et al., 2003)	N/A
OMIM database	OMIM	RRID: SCR_006437 (http://omim.org)
EST database	NCBI EST	RRID: SCR_004630 (https://www.ncbi.nlm.nih.gov/nuccore/)
GEO database	Gene Expression Omnibus	RRID: SCR_007303 (https://www.ncbi.nlm.nih.gov/geo)
NN1.0ext PPI dataset	Source: This paper (Table S2); deposited in IntAct (RRID: SCR_006944, https://www.ebi.ac.uk/intact/) at EMBL-EBI, UK	IntAct: IM-28217
HIPPIE database	Alanis-Lobato et al., 2017	RRID: SCR_014651 (http://cbdm-01.zdv.uni-mainz.de/~mschaefer/hippie/)
UniHi database	Unified Human Interactome (Chaurasia et al., 2007)	RRID: SCR_005805 (http://www.unihi.org)
DrugBank database	DrugBank (Wishart, 2007; Wishart et al., 2006)	RRID: SCR_002700 (http://www.drugbank.ca)
HomoloGene database	HomoloGene	RRID: SCR_002924 (https://www.ncbi.nlm.nih.gov/homologene)
STRING database	STRING	RRID: SCR_005223 (https://string-db.org/)
Blat search genome database	N/A	https://genome.ucsc.edu/cgi-bin/hgBlat
GoldenPath (human genome) database	N/A	https://genome.ucsc.edu/
Gene Ontology (GO) database	Gene Ontology	RRID: SCR_002811 (http://www.geneontology.org/)
Collection of differentially aging-related expressed human genes	Lu et al., 2004	N/A
Collection of HTT-interacting proteins from a Y2H/MS study	Kaltenbach et al., 2007	N/A
Collection of selected NDCPs	This paper (Table S3)	N/A

(*Continued on next page*)

Continued

REAGENT or RESOURCE	SOURCE	IDENTIFIER
Collection of selected ND modifiers	This paper (Table S3)	N/A
HI-II-14 PPI dataset	Rolland et al., 2014	N/A
CORUM (protein complex dataset)	CORUM (Ruepp et al., 2010; Woodsmith and Stelzl, 2014)	RRID: SCR_002254 (https://mips.helmholtz-muenchen.de/corum/)
Phosphosite (kinase-substrate PPI dataset)	PhosphoSitePlus: Protein Modification Site (Hornbeck et al., 2015)	RRID: SCR_001837 (https://www.phosphosite.org/homeAction.action)
Supersaturation scores of human proteins	Ciryam et al., 2013	N/A
Protein set obtained from amyloid plaques	Liao et al., 2004	N/A
Protein set obtained from neurofibrillary tangles (NFTs)	Wang et al., 2005	N/A
Protein set obtained from Lewy bodies	Xia et al., 2008	N/A
Experimental Models: Cell Lines		
E.coli: Competent Mach1 cells	Thermo Fisher Scientific	Cat#C862003
S. cerevisiae: L40ccα [MATα his3Δ200 trp1-910 leu2-3,112 ade2 LYS2::(lexAop)4HIS3 URA3::(lexAop)8-lacZ GAL4 gal80 can1 cyh2]	Wanker et al., 1997; Goehler et al., 2004	N/A
S. cerevisiae: L40ccua [MATa his3Δ200 trp1-901 leu2-3,112 LYS2::(lexAop)4-HIS3 ura3::(lexAop)8-lacZ ADE2::(lexAop)8-URA3 GAL4 gal80 can1 cyh2]	Wanker et al., 1997; Goehler et al., 2004	N/A
Homo sapiens: HeLa cell line	ECACC (Sigma-Aldrich)	Cat#93021013; RRID: CVCL_0030
Homo sapiens: HEK293 cell line	ECACC (Sigma-Aldrich)	Cat#85120602; RRID: CVCL_0045
Experimental Models: Organisms/Strains		
E. coli: OP50 strain	N/A	Acc. No.: PRJNA41499; Tax ID: 637912
D. melanogaster: GMR-GAL4/UAS-TDP-43 M337V	Ritson et al., 2010	Line #1
D. melanogaster: y1w118	Juan Botas (The Hutch, Seattle, USA)	N/A
D. melanogaster: GMRGAL4/CyO	Juan Botas (The Hutch, Seattle, USA)	N/A
D. melanogaster: UAS-Hsap\HTT336Q128[M64]	Juan Botas (The Hutch, Seattle, USA)	N/A
D. melanogaster: Elav-GAL4	Juan Botas (The Hutch, Seattle, USA)	N/A
D. melanogaster: UAS-Hsap\HTT336Q128[F27B]	Juan Botas (The Hutch, Seattle, USA)	N/A
Homo Sapiens: Brain tissues	Institute for Aging and Health, Newcastle University (Newcastle upon Tyne, UK)	N/A
pBTM116-D9 (derived from pBTM116)	Clontech; Goehler et al., 2004	N/A
pACT4-DM (derived from pACT2)	Clontech	Cat#638822
pPA-RL-GW	Trepte et al., 2015	N/A
pFL-V5-GW	Trepte et al., 2015	N/A
pCFPHttex1Q49	This paper	N/A
pV5mCherryLuc	This paper	N/A
pV5ARF-GEP100	This paper	N/A
pTHW	Kaltenbach et al., 2007	N/A
pmTq2-DEVD-mCit	Grünberg et al., 2013	N/A
pGW-RL-PA	Trepte et al., 2015	N/A
pGW-FL-V5	Trepte et al., 2015	N/A
pNL1.1	Promega	#N1001
pcDNA3.1(+)	ThermoFisher	V79020
pDONR221	ThermoFisher	12536017
pDS_X-mCherry	ATCC	MBA-303

(*Continued on next page*)

Continued

REAGENT or RESOURCE	SOURCE	IDENTIFIER
pDONR221-NL	Trepte et al., 2018	N/A
Additional plasmids and more information	Trepte et al., 2018	Dataset EV1
Software and Algorithms		
G2D (candidate genes to inherited diseases) tool	Perez-Iratxeta et al., 2005	RRID: SCR_008190
Genie text mining tool	Fontaine et al., 2011	http://cbdm-01.zdv.uni-mainz.de/~jfontain/cms/?page_id=6
MeSH (medical vocabulary resource)	MeSH	RRID: SCR_004750 (https://www.nlm.nih.gov/mesh/index.html)
Visual Grid software	Agennix AG	N/A
GraphPad Prism	GraphPad	RRID: SCR_002798 (http://www.graphpad.com)
Aida image analysis software	Elysia-Raytest	RRID: SCR_014440 (https://www.elysia-raytest.com/en/cataloglight/c30~aida-mage-analysis-software)
R for statistical computing	R Project for Statistical Computing	RRID: SCR_001905 (https://www.r-project.org/)
Cytoscape software	Shannon et al., 2003	RRID: SCR_003032 (https://cytoscape.org/)
NetworkAnalyzer (Cytoscape plugin)	Assenov et al., 2008	N/A
PRINCE algorithm	Vanunu et al., 2010	N/A
Prediction of protein complexes	Mazza et al., 2016	N/A

RESOURCE AVAILABILITY

Lead Contact

Further information and requests for resources and reagents should be directed to and will be fulfilled by the Lead Contact, Erich Wanker (erich.w@mdc-berlin.de).

Materials Availability

This study did not generate new unique reagents.

Data and Code Availability

The accession number for the binary PPIs of NN1.0ext reported in this paper (*Table S2*) is IntAct: IM-28217. The data have been submitted to the IMEx consortium (http://www.imexconsortium.org) through IntAct [Orchard et al., 2014] and are accessible under https://www.ebi.ac.uk/intact/search/do/search?searchString=pubid:IM-28217.

EXPERIMENTAL MODEL AND SUBJECT DETAILS

Cells, *C. elegans* and *D. melanogaster* models

For plasmid transformation experiments, competent *E. coli* Mach1 cells were routinely grown in flasks or microtiter plates with LB ampicillin medium. Nematodes were maintained on *E. coli* OP50 seeded NGM plates. For transformation with plasmid DNA yeast strains (L40ccua and L40ccα) were grown in rich medium (YPD) supplemented with 2 % glucose. For transient transfection experiments with plasmid DNAs, HeLa cells were cultivated in DMEM medium (Dulbecco's Modified Eagle Medium, GIBCO 31885049) containing L-glutamine, sodium pyruvate and 1 g/l D-glucose, supplemented with 10% FBS and 1% P/S. Cells were incubated at 37°C with 5% CO_2 in cell culture flasks. Then, cells were washed once with PBS and treated with trypsin/EDTA for two minutes, resuspended in medium and centrifuged for three minutes at 150 g. Finally, the cells were seeded into new cell culture flasks, 6-well plates or 96-well microtiter plates according to maintenance or analyses intended.

For RNAi-mediated knockdown experiments nematodes were grown on NGM plates seeded with the *E. coli* HTT115 strains carrying the L4440 plasmid encoding the respective *C. elegans* gene at 20°C. For synchronization, gravid adults from one 10 cm NGM plate were collected in a canonical tube and treated with 20% alkaline hypochlorite solution under vigorous agitation for 4 min. The eggs were then washed 3 times with cold 0.1 M NaCl solution. The eggs were allowed to hatch in M9 medium at 20°C for 22 h.

The *D. melanogaster* strain GMR-GAL4/UAS-TDP-43 M337V (line #1) was previously described (Ritson et al., 2010). Flies were raised on standard diet. RNAi stocks were obtained from either the Bloomington *Drosophila* Stock Center (Indiana University, Bloomington, IN, USA, RRID:SCR_006457) or the Vienna *Drosophila* Resource Center (RRID:SCR_013805). *Drosophila* lines used for RNAi knockdown and co-expression experiments are listed in Table S4.

The fly line for expression of GFP (1521) was obtained from the Bloomington *Drosophila* Stock Center. The fly strains y1w118, GMRGAL4/CyO, UAS-Hsap\HTT336Q128[M64], Elav-GAL4 and UAS-Hsap\HTT336Q128[F27B] were provided by Juan Botas (Fred Hutchinson Cancer Research Center, Seattle, Washington). Transgenic flies harboring HTT partner proteins (Table S4) were generated by BestGene Inc (Chino Hills, CA, USA). For all experiments, flies were kept at 25°C on standard medium. The Information about age and sex of the flies is not available.

METHOD DETAILS

Selection of ND-related target genes

For the selection and prioritization of target genes related to neurodegenerative diseases (NDs), we first generated 15 collections with human genes (see below and Table S1). Targets were selected based on available literature information, high throughput experimental datasets, data mining of genomic and drug target data and text mining of MEDLINE abstracts (https://pubmed.ncbi.nlm.nih.gov/). We focused mainly on five diseases (AD, HD, PD, ALS and SCA1) but did not exclude available information related to other NDs. Finally, using the available information a ranked list of genes related to NDs was generated. Each gene *g* of the collection *c* was scored with a subscore R_{cg} between 0 (not selected or not predicted relation) and 1 (high confidence selection or prediction):

$R_{cg} \in [0,1]$

An overall gene score S_g was computed as a weighted sum of the collection's subscores as

$$S_g = \sum_c W_c^* R_{cg}$$

where the collection weight W_c was defined as shown in Table S1.

When a high throughput dataset of size N (e.g., the total number of probes of a microarray dataset) was analyzed for a collection *c* and returned a p value (Table S1), the subscore R_{cg} of gene *g* was defined as:

$$R_{cg} = \frac{\min\left(-log_{10}(pvalue), -log_{10}\left(\frac{K}{N}\right)\right)}{-log_{10}\left(\frac{K}{N}\right)}$$

For the gene collection ProtAgg_TM the constant $K = 1\ e^{-30}$ was applied; for the gene collections ND_TM, ND_DifExp, ND_DrugT_TM and Aging_DifExp (see details below and in Table S1), we applied $K = 0.05$. Through this data integration strategy, a ranked list of 3,711 potentially ND-associated genes was created (Table S1).

The Known_NDTs selection method is a manual selection by mutations from the literature on the following disease-causing genes known to be related to the key NDs described above (sub score = 1 if selected, 0 otherwise): SNCA, APP, HTT, ATXN1, PARK2, SOD1 and PSEN1. In addition to known disease causing genes, the procedure includes a manual ranking of genes genetically related to NDs from the OMIM database (sub score = 1 if considered very interesting, 0.75 if interesting, 0.5 if moderately interesting, 0.3 if selected and 0 otherwise).

The manual method GenMod was used to select genes from the literature that have mutations associated to NDs (sub score = 1 if selected, 0 otherwise).

With AggToxMod genes known to be disease modulators were manually selected from literature (sub score = 1 if selected, 0 otherwise).

The HTT_Int method is a selection of HTT-interacting proteins from a study using high-throughput yeast two-hybrid screenings and affinity pull down followed by mass spectrometry experiments. The HTT sub score is set to 1 if the gene was listed in the related article (Kaltenbach et al., 2007), 0 otherwise.

The OrthMod method is a selection based on several studies of HD, PD and SCA modulators in human or animal models (mouse, yeast, fly and worm). Relevant genes in a set of selected articles (Table S1, sheet "Studies OrthMod") were extracted and automatically matched to the human orthologs using the Homologene database.

The sub score is set to 1 if the gene is a modifier, listed in the articles and if it has a human ortholog. The sub score is equal to 0 otherwise.

The ND_ChrReg method is a set of gene predictions for the NDs of interest (Table S1, sheet "Datasets") using the G2D tool (Perez-Iratxeta et al., 2005), except SCA1 due to missing information. G2D evaluates genes in the chromosomal region where the disease is mapped to; it prioritizes them for a possible relation to the disease based on the phenotype of the disorder or their similarity to an already known related gene. If a phenotype is linked to multiple loci, known or inferred interactions between proteins of two loci each are also used. The sub score is the resulting gene score of G2D or 0 if the gene has no G2D score.

The ND_TM method used the Génie text mining algorithm of gene prioritization (Fontaine et al., 2011). The query for each disease was done using corresponding MeSH (Medical Subject Headings; NCBI). As no MeSH term is specifically dedicated to SCA1, we used the more general term "Spinocerebellar Ataxias" to produce the results. We selected genes associated to p values below 0.005. The sub

score is a scaling of the returned p value between 0 and 1 (see calculation of R_{cg} above). Score = 1 means that topics of articles related to a gene over-represent at least one of the 5 NDs with very high confidence. Score 0 means that there is no over-representation.

The ND_TissESTs method is based on the EST database to have evidence on gene expression in tissues from the nervous system. We used the GenBank database to select ESTs annotated to be expressed in the nervous system. EST tissue annotations were matched to relevant MeSH terms. We used all MeSH headers and synonymous terms which depend on "Nervous System" (MeSH term ID starts with A08) in the hierarchy. Assignment of ESTs to genes was done by similarity search (Blat) on the human genome (GoldenPath). We selected only hits with high score and percentage of identity (blat score/qSize $\geq$ 95 and pid $\geq$ 95%). The sub score is set to 1 when ESTs were selected, 0 otherwise.

The ND_DifExp method is based on publicly available microarray datasets of ND-related human samples (Table S1, sheet "Microarrays ND_DifExp"). Each dataset was processed to extract differentially expressed genes between healthy and disease patients. No SCA1-related datasets were found in the NCBI Geo database. The score is a scaling of the minimal p value between 0 and 1 (see calculation of R_{cg} above). We selected p values below 0.005. Score 1 means that a gene is considered differentially expressed (over- or under-expressed) with very high confidence. Score 0 means no differential expression.

The DrugBank method is based on the DrugBank database (Wishart et al., 2006) which is a bioinformatics and cheminformatics resource that combines detailed drug data with comprehensive drug target information. At the time of download, the database contained approximately 4,800 drug entries including > 1,350 FDA-approved small molecule drugs, 123 FDA-approved biotech (protein/peptide) drugs, 71 nutraceuticals and > 3,243 experimental drugs. Additionally, more than 2,500 non-redundant protein (i.e., drug target) sequences are linked to these FDA approved drug entries. We have set lists of drugs that target each gene. The specificity of each drug decreases with its number of targets. Each drug related to a gene is scored as follows:

$$Drug\ specificity = \frac{1}{\sqrt{number\ of\ known\ gene\ targets}}$$

The final gene score is the maximum of observed scores of its related drugs. Low scores denote weakly specific drugs and high scores denote very specific drugs.

The ND_DrugSideEff method is based on protein targets prediction of FDA (Food and Drug Administration) approved drugs. Known drug targets were extracted from the manually curated protein-chemicals interaction databases MATADOR, DrugBank and PDSP Ki databases. The prediction is based on a scoring scheme that evaluates the probability that a drug shares a direct target with known PD-, AD- or ALS-related drugs. The scoring scheme is calculated given the similarity of side effects and the Tanimoto's 2D structural similarity index. The sub score of a gene is the maximal value of the specificity of its predicted drugs that is calculated as defined in the DrugBank method (see above). Scores are between 0 (bad) and 1 (good).

The ND_DrugT_TM method scores each human gene thanks to a list of drugs related to the gene and to NDs by using text mining of MEDLINE abstracts. We have used a list of known ND drugs and related disease targets from DrugBank (Table S1, sheet "Drugs ND_DrugT_TM"). The best drug-ND associations were first evaluated and selected by Fisher's exact tests (p values < 0.005) based on co-occurrences of ND-related MeSH terms and drug names in Medline abstracts. P values were scaled from 0, no association to 1, strong association (see calculation of R_{cg} above). Scores were multiplied by the drug specificity (as defined in the DrugBank method). Then, the final gene score is the maximum of observed scores of its related ND drugs.

The ProtAgg_TM method used the Génie text mining algorithm (Fontaine et al., 2011) to predict human protein-coding genes related to protein aggregation. The training set was composed of abstracts related to protein aggregation from a PubMed query and compared to the rest of MEDLINE (Fontaine et al., 2011). The method selected 992 genes with uncorrected p values ranging from $1*10^{-5}$ to $1.55*10^{-158}$. The sub score was defined as the scaling of the p value (see calculation of R_{cg} above) so that a score 1 means very high confidence and score 0 means that there is no over-representation.

The IntGenMod method is based on Known_NDTs genes and used the UniHi database (http://www.unihi.org) to find interacting proteins and the STRING database (https://string-db.org) to discover functionally related genes. We manually defined a scoring scheme for UniHi genes that considers the number of related direct and indirect interactors within Known_NDTs genes, and a scoring scheme for STRING genes that depends on the number of interactors (Table S1, sheet "Scores IntGenMod"). Genes showing direct interactions in UniHi with one or several Known_NDTs genes received the highest scores. A search in STRING was done for the best 27 Known_NDTs genes that have a sub score $\geq$ 0.5. The overall score is the maximum of UniHi and STRING gene scores.

The Aging_DifExp method is based on genes differentially expressed between young (age $\leq$ 42 years) and older (age $\geq$ 73 years) people from a gene list provided in a published study (Lu et al., 2004). Post-mortem samples from the frontal pole of 30 individuals ranging in age from 26 to 106 were analyzed using Affymetrix gene chips. The score is a discretization of the provided q-values. Score 1 corresponds to a q-value equal to 0 and score 0.8 to a p value equal to 0.01. Score 0 means no differential expression.

Literature review for selected target genes

Text mining for the top 100 of the initially selected targets for the term "neurodegeneration" was done using the Génie algorithm (Fontaine et al., 2011). We assessed how often each of the selected target genes was found together with the term "neurodegeneration" in previously published scientific abstracts.

Enrichment analysis

Enrichment of binary interactome maps [NN1.0, NN1.0ext and HI-II-14 (Rolland et al., 2014)] for functional relationships [shared Gene Ontology (GO) terms] and co-complex memberships was determined. In addition, the number of known kinase-substrate interactions found in the binary interaction maps was investigated.

The published datasets (Ruepp et al., 2010; Woodsmith and Stelzl, 2014) and (Hornbeck et al., 2015) were used for analysis. PPIs were trimmed to interactions where both proteins were present in the binary interactome maps for pairwise comparisons. The enrichment was computed as the hypergeometric p value of the intersection between the examined PPI set and a gold standard set (Figure 2A).

Prediction of disease-relevant proteins

To predict potential disease-relevant proteins such as NDCPs, ND modifiers or drug targets in NN1.0ext, a network propagation algorithm was applied (Mazza et al., 2016; Vanunu et al., 2010). This approach starts from primarily defined priors (e.g., known NDCPs) and a single initial parameter (alpha) that weighs the contribution of the network versus that of the priors. Here, we used a default parameter alpha of 0.9 as recommended (Gottlieb et al., 2011; Vanunu et al., 2010). This value gives more weight to the network over the prior values.

A quantitative propagation score for every protein in the network was calculated, which is an indication of its proximity to the prior proteins. This scoring provides a ranking of the proteins, which we can evaluate using a receiver operating characteristic (ROC) curve (Figures 2B–2D). To assess the significance of the ROC curve obtained, we compared it to 100 analogous curves that result from applying the same procedure to 100 randomized networks with the same node degrees.

It should be noted that the propagation scores correlate with the vertex degree that is highest for the baits of the Y2H experiment. Since these baits were chosen to be ND related, they intersect the lists of NDCPs and ND modifiers that are shown in the Figures 2B and 2C.

Construction of ND subnetworks and modules

Subnetworks and protein modules for the NDs AD, PD and ALS were constructed using a previously described propagation-based algorithm (Mazza et al., 2016). Briefly, the computation starts from known priors (NDCPs, Table S3), which are available in the literature for each disease. The network's proteins are then ranked with respect to the prior set using propagation, and their scores are compared to those obtained by propagating random prior sets of the same size. By ranking the real score of every protein against its random counterparts (excluding the random instances where this protein was selected as the prior), we obtained an empirical p value for every protein in NN1.0ext, retaining only those at a 0.01 significant level. The generated PPI subnetworks were termed AD_{SN}, PD_{SN} and ALS_{SN}. The subnetworks induced on these significantly scoring proteins served as the input network for the prediction of highly connected protein clusters (Mazza et al., 2016), here also termed AD_{MO}, PD_{MO} and ALS_{MO} (Figures 4D–4F). High scoring clusters were detected using an integer linear programming algorithm (Mazza et al., 2016) that optimizes the interaction density of a candidate module as well as the scores of its member proteins. This process resulted in 4-5 protein clusters for each disease using the available PPI information (Figures 4D–4F and S4A).

Data cross-comparisons

For systematic data cross-comparisons, we merged the genes of our computationally predicted disease subnetworks AD_{SN}, PD_{SN} and ALS_{SN} into one dataset. This dataset was then compared with published data from Na et al. (2013) and Chen and Burgoyne (2012). In both publications so-termed genetic modifiers, i.e., genes that influence ND-related phenotypes in disease models such as *C. elegans, D. melanogaster* and yeast were compiled in comprehensive datasets. We then mapped these genes to their human orthologs and defined those that are present in NeuroNet1.0ext. Next, we determined the overlaps between our computationally predicted gene set and the previously reported datasets (Na et al., 2013; Chen and Burgoyne, 2012; Figure 4A). To evaluate whether the observed overlaps can be expected by chance, we performed a hypergeometric test, indicating that potential genetic modifiers are significantly enriched in our computationally predicted protein subnetworks (p values < 0.01; Figure 4B).

Next, we investigated whether proteins that aggregate in patient brains are enriched in our disease-associated subnetworks. We compared this dataset with related published data from Liao et al. (2004), Wang et al. (2005) and Xia et al. (2008); here, proteins associated with amyloid plaques, neurofibrillary tangles and Lewy bodies were identified.

We found that 117 (15.4 %) out of the 762 proteins, which are aggregated in AD and PD patient brains, are present in our computationally predicted disease-associated subnetworks (Figures 5C–5E). To assess whether this overlap can be expected by chance, a hypergeometric test was performed using the protein set of NN1.0ext as the protein universe. It revealed that potential aggregation-prone proteins are significantly enriched in our predicted disease subnetworks (p value < 0.0001).

For the identification of disease-associated proteins, we first merged the proteins of our computationally predicted disease modules AD_{MO}, PD_{MO} and ALS_{MO} into one dataset. In addition to priors (Figure 4G), i.e., known NDCPs that were initially utilized for module identification, our protein modules contain 56 non-prior proteins. These proteins were then mapped to the OMIM database containing information for multiple genetic disorders. We found that 24 (42.9 %) proteins are present in OMIM. They were termed OMIM disease-associated proteins (ODAPs, Figure 4H). To evaluate whether such a high number of proteins can be expected

by chance, we performed a hypergeometric test using NN1.0 as the protein universe. This analysis indicated that ODAPs are significantly enriched in our computationally predicted protein modules (p value < 0.0001).

Supersaturated, aggregation-prone proteins

Based on the database provided by Ciryam et al. (2013), that contains supersaturation scores assigned to proteins of the human proteome, we compared the average supersaturation score of the whole proteome with the average score of the predicted proteins in the subnetworks and modules. The supersaturation score σ_f measures the aggregation tendency of proteins that are initially folded, while the supersaturation score σ_u measures that of unfolded proteins. We calculated the median of the supersaturation scores for the proteome and the proteins in the predicted disease-specific subnetworks and protein modules. The statistical significance was assessed by the Mann-Whitney U test with Bonferroni-corrected p values. GraphPad Prism (GraphPad, RRID:SCR_002798) was used to create the boxplots. They extend from the lower to the upper quartiles, with the internal lines referring to the median values (Figures 5A and 5B).

To investigate the abundance of co-aggregating proteins from ND patient brains in our predicted subnetworks, we analyzed protein sets obtained from amyloid plaques (Liao et al., 2004), neurofibrillary tangles (NFTs) (Wang et al., 2005) and Lewy bodies (Xia et al., 2008). For comparison, the abundance of the patient brain proteins in the proteome was also analyzed. The statistical significance was assessed with a Fisher's exact test with Holm–Bonferroni corrections (Figures 5C–5E).

Automated Y2H interaction screening

The MATα yeast strain L40ccα was individually transformed with pACT4-DM-based plasmids encoding prey proteins to create a prey-matrix for interaction mating. The resulting yeast clones were arrayed in 384-well microtiter plates. The pBTM116-D9-based plasmids encoding bait proteins were transformed into the MATa yeast strain L40ccua. The activation of the reporter genes *HIS3*, *URA3*, and lacZ through the production of bait proteins (autoactivation tests) was investigated systematically. Only yeast strains that express reporter non-autoactivating bait proteins were utilized for systematic interaction screening (Stelzl et al., 2005). Liquid cultures of MATα yeast strains (preys) were replicated in 384-well microtiter plates using a pipetting robot (Tecan Freedom EVOware) and mixed with MATa strains expressing bait proteins. Then, yeast mixtures were transferred onto YPD agar plates for interaction mating using a spotting robot (Kbiosystems K4). After incubation for 48 h at 30°C, the resulting colonies were automatically picked from agar plates and transferred into 384-well microtiter plates containing SDII (-Leu-Trp) liquid medium. From these plates, they were spotted onto SDII (-Leu-Trp) agar to select for diploid yeasts carrying both – bait and prey - vectors. After additional incubation for 48 h at 30°C, diploid yeast clones were spotted onto SDIV (-Leu-Trp-Ura-His) agar to detect PPIs through growth selection. In addition, yeast clones were spotted onto high density Nylon membranes placed on top of SDIV agar plates to perform β-galactosidase assays. After incubation for 3 to 4 days at 30°C, grown colonies were fractured by liquid nitrogen and β-galactosidase activity was determined using X-Gal as a substrate. Digital images were taken from agar plates and from high density Nylon membranes and analyzed using the Visual Grid software (GPC Biotech).

PPI detection in cells using DULIP and LuTHy

The procedure for detecting binary PPIs in mammalian cells using DULIP has been described in detail (Trepte et al., 2015). Briefly, HEK293 cells (ECACC, Cat#85120602, RRID:CVCL_0045) were reversely transfected in 96-well microtiter plates at a density of 3.75×10^4 cells per well. 48 hours post transfection, cells were lysed in 100 μL HEPES lysis buffer [50 mM HEPES, 150 mM NaCl, 10% glycerol, 1% NP-40, 0.5% deoxycholate, 20 mM NaF, 1.5 mM $MgCl_2$, 1 mM ethylenediaminetetraacetic acid, 1 mM DTT, 1 U Benzonase, protease inhibitor cocktail (ethylenediaminetetraacetic acid free; Roche) and 1 mM PMSF] for 30 min at 4°C. Production of luciferase-tagged fusion proteins was monitored by measuring the respective activities in crude cell lysates in 384-well microtiter plates. 10 μL of cell lysate was added to 20 μL phosphate-buffered saline (PBS), and 10 min after the addition of 10 μL Dual-Glo luciferase reagent (Promega), the firefly activity (FL_{IN}) was measured using an Infinite

M1000 (Tecan) plate reader. To stop the FL activity and to measure the RL activity (RL_{IN}), we added 10 μL of the Dual-Glo Stop and Glo reagent (Promega) and measured the activity after 15 min of incubation. In parallel, 50 μL of the cell lysate was incubated for 3 h at 4°C in IgG pre-coated 384-well microtiter plates. Plates were coated with sheep gamma globulin (Dianova), blocked with 1% bovine serum albumin in carbonate buffer (70 mM $NaHCO_3$ and 30 mM Na_2CO_3, pH 9.6) before they were incubated with rabbit anti-sheep IgGs (Jackson ImmunoResearch Labs Cat#313-005-003; RRID:AB_2339937) overnight. After cell lysate incubation, all wells were washed three times with HEPES lysis buffer before 30 μL of PBS was added to each well. Measurement of firefly (FL_{OUT}) and *Renilla* (RL_{OUT}) luminescence activity was performed as described above using an Infinite M1000 (Tecan) plate reader.

The double-readout bioluminescence-based two-hybrid technology (LuTHy) for testing binary interactions has been described (Trepte et al., 2018). Reverse transfection of HEK293 cells in white 96-well microtiter plates (Greiner, 655983) at a density of 4.0–4.5 $\times 10^4$ cells per well was performed. Plasmids encoding donor and acceptor proteins were transfected at a 1:10 to 1:20 ratio, with 5–10 ng DNA for the donor and 100 ng for the acceptor. The fluorescence of mCitrine was measured 48 h after transfection in intact cells (Ex/Em: 500 nm/530 nm). Then, coelenterazine-h (NanoLight, 301 or pjk, 102182) was added to a final concentration of 5 μM. The cells were incubated for an additional 15 min and the total, short-WL and long-WL luminescence was measured. Here, fluorescence and luminescence were measured using the Infinite microplate readers M200, M1000, or M1000Pro (Tecan) using the BLUE1 (370–480 nm) and the GREEN1 (520–570 nm) filters at 1,000 ms integration time. After this step, luminescence-based

co-precipitation (LuC) was performed. Production of PA-mCit- and NL-tagged fusion proteins was monitored by measuring fluorescence (mCitIN) and luciferase activity (NLIN) in crude cell lysates in white, small volume 384-well microtiter plates (Greiner, 784074). We added 5 μl coelenterazine-h to 5 μl of cell lysates to a final concentration of 10 μM and measured the luminescence activity as before in a microplate reader with 100 ms integration time. We coated small-volume 384-well microtiter plates (Greiner, 784074) the day before use with sheep gamma globulin (Jackson ImmunoResearch, 013-000-002) in carbonate buffer (70 mM NaHCO3, 30 mM Na2CO3, pH 9.6) for 3 h at room temperature. Then, 15 μl cell lysate was incubated for 3 h at 4°C in the IgG-coated 384- well plates. Wells were washed 3 times with lysis buffer and mCitrine fluorescence (mCitOUT) was measured as above. Finally, 15 μl of PBS buffer containing 10 μM coelenterazine-h was added to each well and the luminescence activity (NLOUT) was measured as described above.

Selection of predicted AD-associated proteins

We created a list of all proteins of the AD module using Microsoft Excel and added random numbers. Based on these numbers, we randomly selected 15 proteins for validation experiments. After eliminating proteins for which no specific antibodies could be identified by SDS-PAGE and immunoblotting (Table S6), 7 remaining proteins and 3 control proteins were assessed by filter retardation assays.

Selection of predicted TDP-43 modulators

We created a list of all TDP-43 interacting proteins from the Y2H studies using Microsoft Excel and added random numbers. Based on these numbers we randomly select 20 proteins for the validation experiments. After sorting the list for these numbers and eliminating known TDP-43 modulators, 15 remaining proteins were assessed experimentally.

Knockdown of target genes in *D. melanogaster*

We conducted our RNAi screen in a *Drosophila* model expressing TDP-43 with the mutation M337V under the control of the GMR-Gal4 driver. The genotype for these transgenic flies has been described (Ritson et al., 2010). Phenotypic analysis of the *Drosophila* eye was performed by crossing the TDP-43 flies to double-stranded UAS-RNAi lines (obtained from the Vienna *Drosophila* Resource Center). A total of 136 genes were selected for modifier screening. This includes 77 genes from the NN1.0ext interaction dataset and 78 TDP-43 interaction partners from a previously published study (Freibaum et al., 2010), of which 19 were also identified in NN1.0ext. In total, 232 RNAi lines were systematically screened (1-3 RNAi lines per gene). Eye degeneration phenotypes were scored on a scale from 0-14 with 7 representing the basal phenotype. Phenotypes were examined 24-48 h after eclosion (Figures 3B and 3C).

Knockdown of target genes in *C. elegans*

For RNAi-mediated knockdowns of target genes, nematodes were placed as L1 larvae onto RNAi plates (containing 1 mM IPTG) and moved onto fresh plates every second day to separate them from their progeny. The aggregation-propensity of disease-associated polypeptides tagged with fluorescent proteins (e.g., TDP-43-M337-YFP, SYN-YFP, Q35-YFP or Luciferase_R188Q_R216Q-YFP) was assessed by fluorescence microscopy 1-5 days after the knockdown of target genes with RNAi was initiated. For imaging, nematodes were mounted onto 2% agarose (Sigma) pads on glass slides and immobilized with 2 mM Levamisole (Sigma). DAPI staining was carried out immediately before mounting the nematodes by incubating them in DAPI solution (final concentration: 100 ng/ml) for 30 min. Images were taken on a Leica SP5 and a Zeiss LSM780 confocal microscope.

Analysis of retina degeneration in flies

For analysis of retina degeneration (Stroedicke et al., 2015) heads of 2-3 day old females were fixed for 48 h in Bouin's fixative (Sigma-Aldrich, St. Louis, MO, USA). Vertical 10 μm semi-thin paraffin sections were produced without histological staining. The absolute retina extension was measured using standard light microscopy. 5-29 females were analyzed per genotype.

Protein aggregates in patient brains

Human postmortem brain tissue samples were obtained from the Newcastle Brain Tissue Resource (NBTR), Newcastle University, UK. Frozen tissue derived from temporal cortex was weighted and homogenized in a 10-fold excess (w/v) of ice cold 50 mM Tris-HCl pH 7.5, 150 mM NaCl, 0.1% SDS, 0.5% sodium deoxycholate, 1% Triton X-100, 0.25 U/μl Benzonase and a complete protease inhibitor cocktail using a schuett homogen plus (schuett-biotec GmbH, Germany) semi-automatic homogenizer (700 rpm). After incubating the homogenate for 30 min at 4°C with rotation, it was centrifuged for 20 min at 1,500 x g at 4°C to remove cell debris. The supernatant was then transferred to a new tube and the protein concentration was determined with the Pierce BCA assay (Thermo Fisher Scientific, Germany) using BSA as a standard. For analysis with filter retardation assays, protein homogenates prepared from frozen brain tissues of AD patients and healthy controls were filtered through a cellulose acetate membrane with a pore size of 0.2 μm (GE Healthcare Life Sciences, Germany). After washing the membrane with 1x PBS (13.7 mM NaCl, 0.27 mM KCl, 1 mM Na_2HPO_4, 0.2 mM KH_2PO_4, pH 7.4), it was blocked for 30 min with 3% skimmed milk (Sigma-Aldrich, Germany) in 1x PBS containing 0.05% Tween-20 (PBS-T). Then, the membrane was incubated over night with the primary antibody diluted in 3% skimmed milk PBS-T. Subsequently, the membrane was washed 3 times for 10 min in PBS-T, incubated for 15 min in 3% H_2O_2 and washed 3 times for 5 min in PBS. Then, the membrane was incubated with the secondary peroxidase-conjugated anti-mouse antibody for 1 h at

room temperature and washed twice for 5 min in PBS-T and twice for 10 min in PBS; immunoreactive protein was finally detected using ChemiGlow (Biozym Scientific GmbH, Germany). Chemiluminescence was detected with a FujiFilm LAS-3000 imager and images were quantified using the Aida image analysis software (Elysia-raytest, Germany, RRID:SCR_014440).

For the detection and quantification of CFP-Httex1Q49 aggregates in HeLa cells (ECACC, Cat#93021013; RRID:CVCL_0030) they were washed once with PBS and lysed in buffer containing 50 mM Tris pH 8, 1 mM EDTA, 100 mM NaCl, 5 mM $MgCl_2$, 1% NP40, protease inhibitor cocktail and benzonase. Then, 30 μl of each cell lysate (20 μg of total protein) was supplied to cellulose acetate membrane in triplicates, filtered and washed with 100 μl of 0.1% NP40. Membranes were blocked for 30 minutes in 3% milk-PBS-0.05 % Tween-20 at room temperature. Incubation of membranes with primary antibodies (anti V5 or anti GFP) was carried out at 4°C with mild shaking overnight, whereas the secondary POD-labeled antibody was applied for 1 h at room temperature. For quantification of chemiluminescence signals, the Aida image analysis software was utilized (Raytest, Germany).

Knockdown of MO2B7.5 (IQSEC1) in *C. elegans*

The gene knockdown was repeated in two independent experiments as described above. Worms were collected, RNA was prepared and used for Real Time PCR to determine the amounts of MO2B7.5 transcripts in control and RNAi treated animals. The results are shown in Figures S3D and S3E.

qRT-PCR with RNAi treated *C. elegans* strains

The Bristol N2 strain was grown on RNAi plates supplemented with 1 mM IPTG, and seeded with HT1551 *E. coli* expressing either ds RNA against *IQSEC1* (Ahringer library gene: M02B7.5, Source BioScience) or the empty vector L4440, as a control. Nematodes were synchronized via alkaline hypochlorite treatment and left to grow until gravid adulthood, approximately 4 days at 20°C. On day 4, nematodes were washed off plates and washed 3 times in M9. After supernatant removal, nematode pellets were snap frozen in liquid nitrogen and stored at −80°C. For RNA extraction worm pellets were thawed on wet ice. To disrupt the cuticle of the worms the freeze-thaw cycle was repeated five times, followed by disruption of the worm pellet by a 19-gauge syringe. Total RNA was extracted using Trizol reagent (Invitrogen/Thermo Fisher Scientific, Waltham, MA, USA) and the NucleoSpin RNA kit (Macherey-Nagel, Düren, Germany) as described (Kirstein et al., 2017). Two μg of RNA was reverse-transcribed using the High-Capacity cDNA Reverse Transcription Kit (Applied Biosystems/Thermo Fisher Scientific, Waltham, MA, USA). For quantitative RT-PCR, 10 ng of cDNA was incubated with 6 μl SYBR Green PCR Master Mix (Applied Biosystems/Thermo Fisher Scientific, Waltham, MA, USA) and 3.96 pmol per primer in a total volume of 12 μl. The following primers were used:

IQSEC1 (Pair 1): 5′-GGTGGAATGCAACTGGCTC-3′ (forward) and 5′-CTCCGCATCTTGCATCGAG-3′ (reverse);
IQSEC1 (Pair 2): 5′-GTGCTCGAGCGAAGATATGG-3′ (forward) and 5′-CATAATACAGTACTCGCGCCACG-3′ (reverse);
cdc-42 (control gene): 5′-AAACTTGTCTCCTGATCAGCT-3′ (forward) and 5′-TACTGTGACGGCGTAATTGT-3′ (reverse).

Real-time PCR was performed using the ViiA 7 real-time PCR system (Applied Biosystems). Samples were measured in triplicates and normalized to the *cdc-42* housekeeping gene. Quantification was performed using the ΔCt method and the QuantStudio real-time PCR Software v1.3.

Co-transfection of HeLa cells

Reverse transfection was applied in a 96-well plate format. For single and co-transfection experiments, 200 ng of each plasmid (pCFPHttex1Q49, pV5mCherryLuc or pV5ARF-GEP_{100}) were used per well. 0.825 μl PEI (stock concentration of 10 mg/ml) was mixed in 1 mL OptiMEM, appropriate amounts of plasmids were added and incubated for 20 min at room temperature. 50 μl of these mixtures were split into triplicates and $6x10^4$ cells were spread in 150 μl growth medium per well.

QUANTIFICATION AND STATISTICAL ANALYSIS

GraphPad Prism, Cytoscape (RRID:SCR_003032), MS-Excel and R (R Project for Statistical Computing, RRID:SCR_001905) were used for data analysis and graphical representation. Statistical parameters including the value of n (number of independent experimental replications), the definition of precision measures arithmetic mean ± SEM along with the significance are reported in the figures and figure legends. Data were judged to be statistically significant when $p < 0.05$ (*), $p < 0.01$ (**), $p < 0.001$ (***) and $p < 0.0001$ (****). Specified statistical tests are described in the method details.

Cell Reports, Volume *32*

Supplemental Information

Interactome Mapping Provides a Network of Neurodegenerative Disease Proteins and Uncovers Widespread Protein Aggregation in Affected Brains

Christian Haenig, Nir Atias, Alexander K. Taylor, Arnon Mazza, Martin H. Schaefer, Jenny Russ, Sean-Patrick Riechers, Shushant Jain, Maura Coughlin, Jean-Fred Fontaine, Brian D. Freibaum, Lydia Brusendorf, Martina Zenkner, Pablo Porras, Martin Stroedicke, Sigrid Schnoegl, Kristin Arnsburg, Annett Boeddrich, Lucia Pigazzini, Peter Heutink, J. Paul Taylor, Janine Kirstein, Miguel A. Andrade-Navarro, Roded Sharan, and Erich E. Wanker

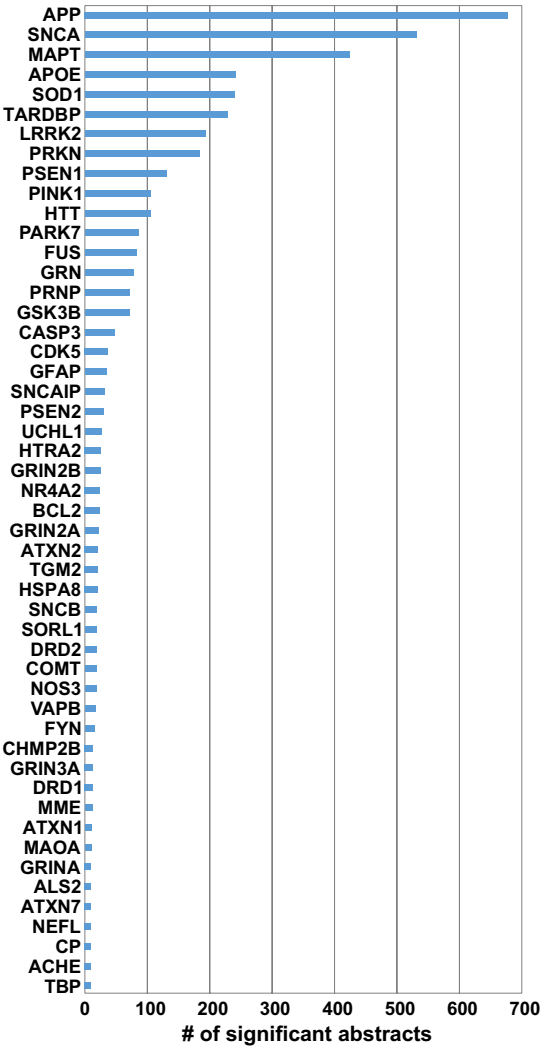

Figure S1. Related to Figure 1. Text mining for initially selected targets
Number of significant abstracts retained from a literature search using the Génie text mining algorithm (Fontaine et al., 2011) for the top 50 of the initially selected targets. We searched for abstracts that contain both a selected target gene as well as the search term "neurodegeneration". Only a relatively small fraction of the selected target genes (~ 20) has been extensively described in the context of neurodegenerative diseases.

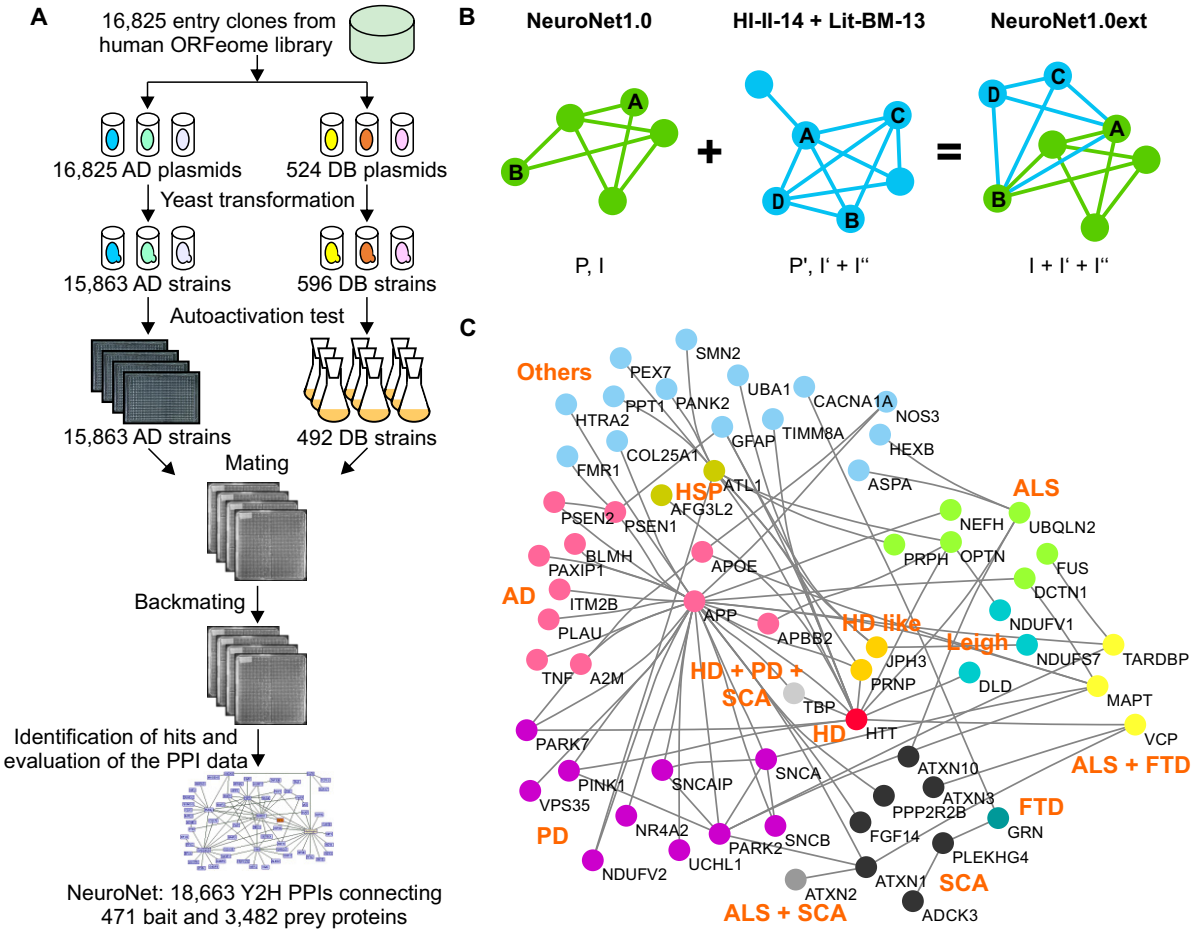

Figure S2. Related to Figure 1. Identification of PPIs and integration of binary Y2H interaction data sets
(A) Simplified workflow depicting the automated Y2H interaction mating technology. DB, DNA binding domain; AD, activation domain.
(B) Scheme depicting the integration of binary Y2H interaction data. The Y2H interactions identified in this study (NN1.0) were extended with previously published high-quality PPIs (Lit-BM-13 and HI-II-14) to generate NN1.0ext. The following PPI integration strategy was applied: Let P be the set of proteins (e.g., A, B) in NN1.0 and let I denote its set of interactions. Let P' be the set of proteins (e.g., C, D) in the Lit-BM-13 and the HI-II-14 collections that have at least two PPIs (e.g., C-A, C-B, D-A, D-B) to proteins in P. Let I' be the set of interactions from the Lit-BM-13 and the HI-II-14 collections that connect proteins in P' to proteins in P or P'. Finally, let I'' be the set of interactions from the Lit-BM-13 and the HI-II-14 collections that connect proteins in P. Then, NN1.0ext is the union of I, I' and I''.
(C) A subnetwork obtained from the NN1.0ext data set depicting interactions between known NDCPs. The network suggests that NDs are related at the molecular level.

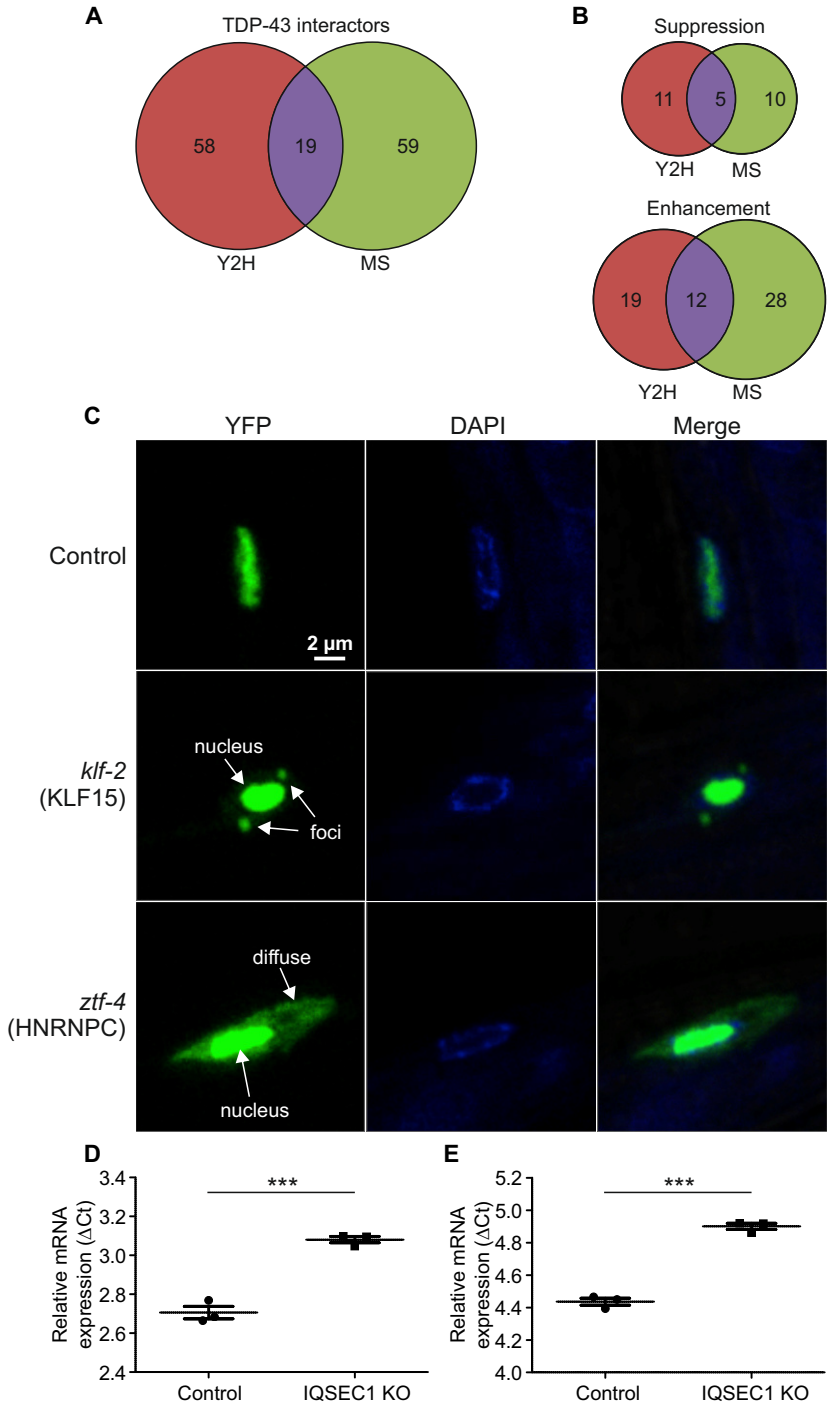

Figure S3. Related to Figures 3 and 6. Investigating the disease relevance of NN1.0ext PPIs in transgenic fly and worm models

(A) Overlap between TDP-43 interacting proteins that were tested with RNAi knockdown experiments in TDP-43-M337V expressing transgenic flies; Y2H, interacting proteins identified with Y2H assays; MS, interacting proteins identified by affinity purification followed by mass spectrometry.

(B) Results from RNAi screens. The impact of partner proteins identified by Y2H assays and affinity purification followed by mass spectrometry (MS) on a TDP-43-M337V-induced rough-eye phenotype in *Drosophila* was systematically assessed.

(C) Cellular TDP-43-M337V-YFP localization phenotype resulting from RNAi knockdown of target genes in a transgenic *C. elegans* model. Observed phenotypes are exemplarily shown. Through the RNAi knockdown of target genes, the translocation of TDP-43-M337V-YFP from the nucleus into the cytoplasm was increased compared to controls, which show exclusively nuclear staining.

(D-E) Quantification of M02B7.5 (IQSEC1) transcript amounts using real-time PCR. RNA was prepared from control and RNAi-treated worms. For PCR two different primer pairs for detecting M02B7.5 transcripts were used. Values were normalised to the cdc42 housekeeping gene. Statistical analysis was performed using the unpaired two-tailed t-test (***$p < 0.001$).

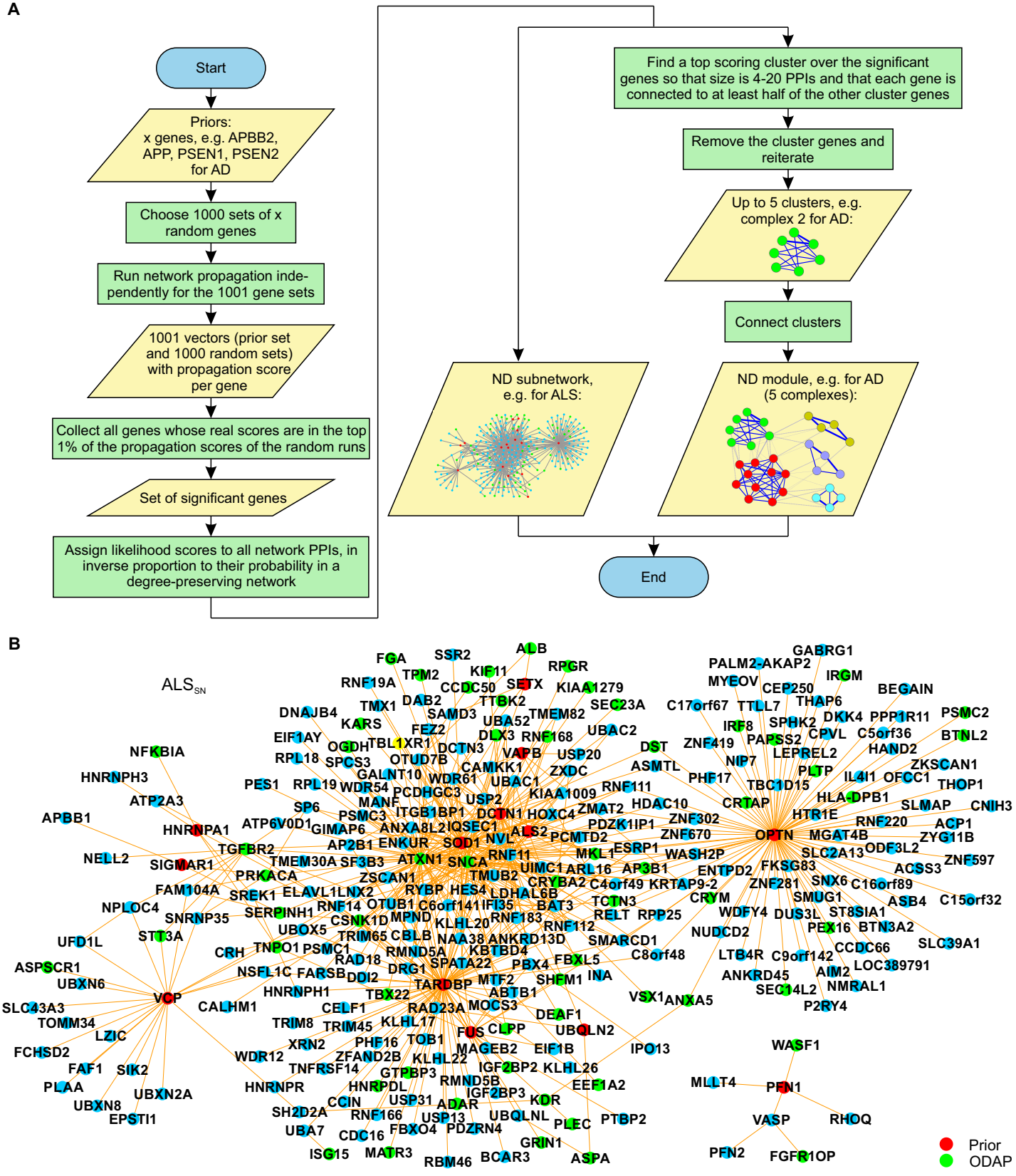

Figure S4. Related to Figures 4 and 5. Computational prediction of ND-relevant protein subnetworks and modules

(A) Workflow depicting the procedure for the computational prediction of ND-specific protein modules and subnetworks from NN1.0ext with network propagation starting from disease-causing proteins (NDCPs, priors); The procedure revealed highly connected protein clusters for the diseases AD, PD and ALS.

(B) The subnetwork ALS_{SN} contains 538 PPIs connecting 283 proteins. It includes 13 known ALS-associated NDCPs that were used as 'priors' for network prediction (in red) as well as 59 further known disease-associated proteins (ODAPs) referenced in OMIM (in green).

(C) Representation of priors (known NDCPs) in computationally predicted ND subnetworks.

(D) Representation of other known disease-associated proteins (ODAPs, based on available OMIM data) in computationally predicted ND subnetworks. Priors (known NDCPs) utilized for subnetwork prediction were not counted.

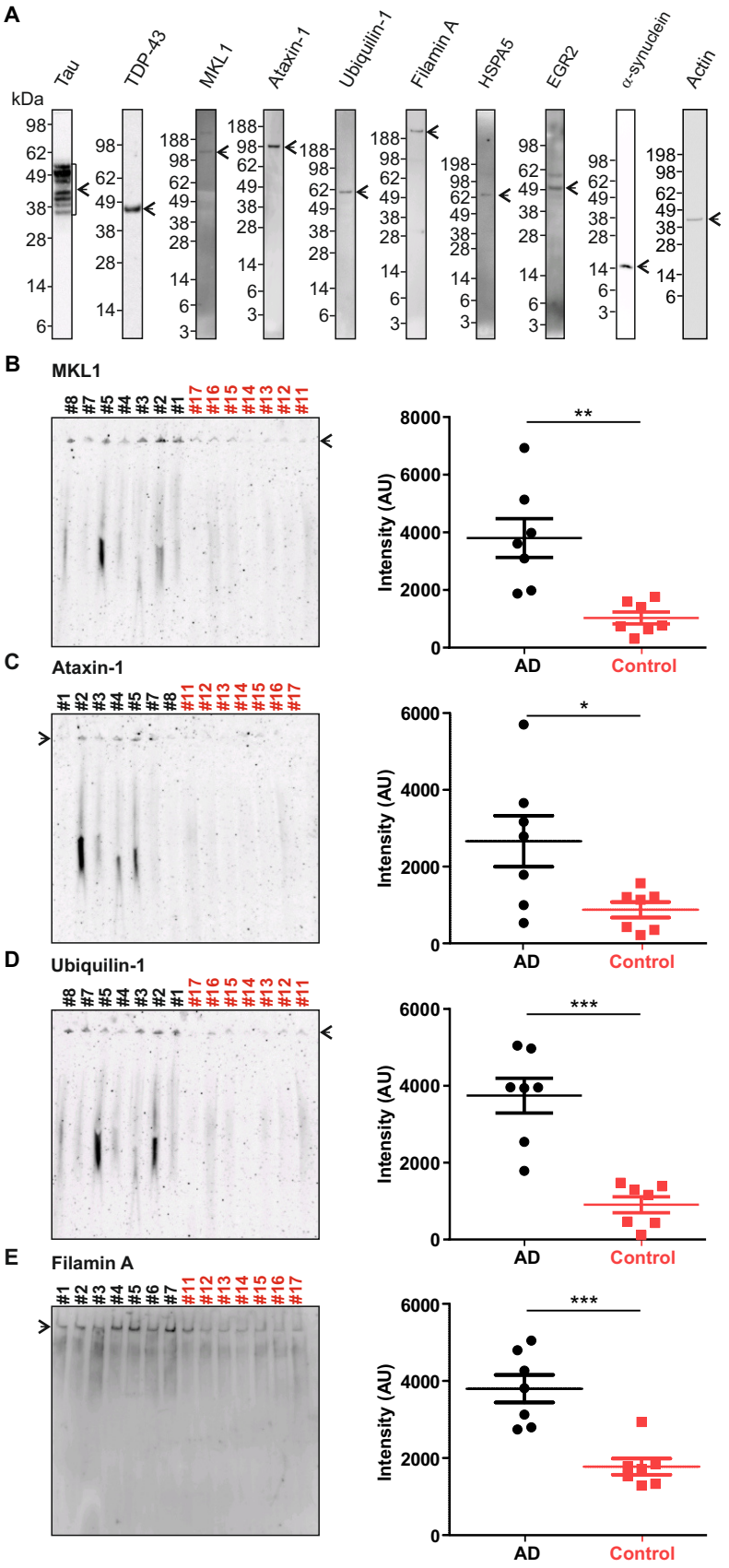

Figure S5. Related to Figure 5. Detection of aggregated proteins in AD patient brains
(A) Western blot analysis. 10 µg of human brain homogenates derived from control individuals were analysed by a denaturing NuPAGE gel and Western blotting using protein specific antibodies. Arrows indicate the detected proteins with their predicted sizes.
(B-E) Analysis of brain extracts by native PAGE. 10 µg of human brain homogenates derived from 7 AD patients (#1-8, black lettering) and 7 control individuals (#11-17, red lettering) were analysed by native PAGE and Western blotting using antibodies against (B) MKL1, (C) ataxin-1, (D) ubiquilin-1 and (E) filamin A. Intensities of high-molecular-weight protein aggregates in gel pockets (arrow) were quantified using the ImageJ software and are shown in arbitrary units (AU) (***$p < 0.001$, **$p < 0.01$, *$p < 0.05$, unpaired two-tailed t-test).

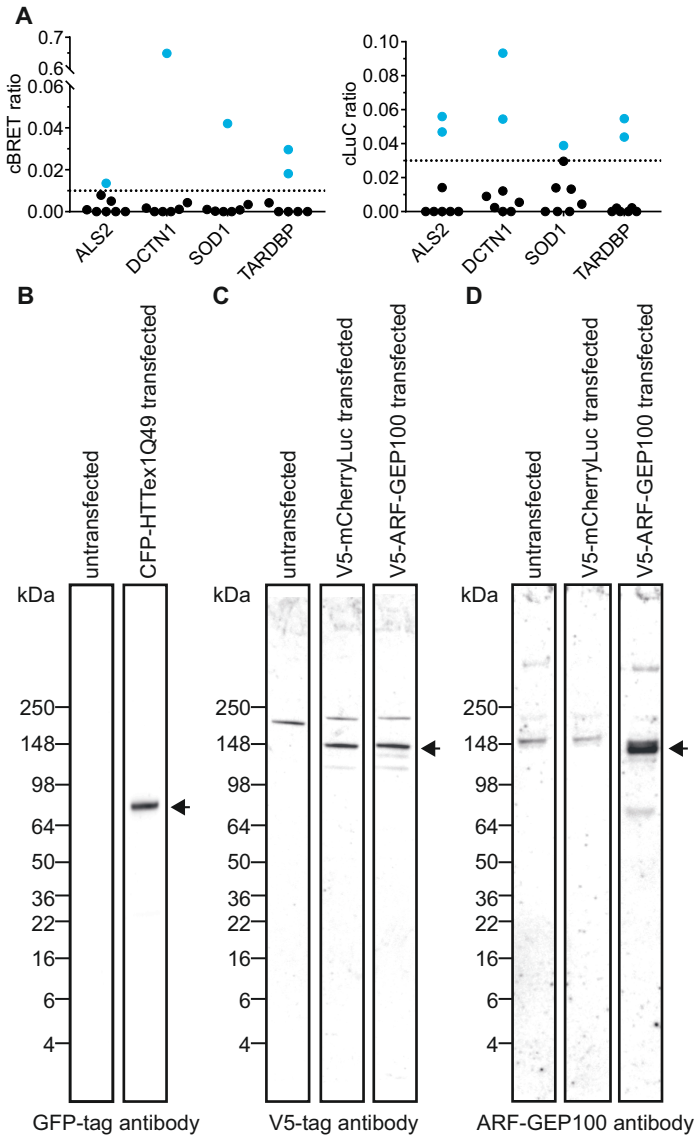

Figure S6. Related to Figures 1, 4 and 6. Systematic analysis of PPIs from the predicted ALS module and of the effect of ARF-GEP100 on CFP-HTTex1Q49 aggregation.

(A) Interacting proteins of ARF-GEP100 from the ALS module were co-expressed as N- and C-terminally tagged NL and PA-mCit fusion proteins in eight different orientations in HEK293 cells. For all orientations cBRET and cLuC ratios were calculated; values (colored in cyan), which are equal or above the thresholds of 0.01 and 0.03, respectively, indicate positive PPIs.

(B-D) Analysis of V5-tagged ARF-GEP100 on CFP-HTTex1Q49 aggregation in HeLa cells by SDS-PAGE and immunoblotting.